Materials & Design 224 (2022) 111292

Contents lists available at ScienceDirect

Materials & Design

journal homepage: www.elsevier.com/locate/matdes

Static assessment of flawed thin AlSi10Mg parts produced by Laser Powder Bed Fusion

G. Minerva, L. Patriarca, S. Foletti, S. Beretta *

Politecnico di Milano, Department of Mechanical Engineering, via La Masa 1, 20156 Milano, Italy

HIGHLIGHTS

- Analysis of the static assessment of thin and flawed AM parts made of AlSi10Mg.
- Assessment must consider elasto-plastic behaviour even if material is quasi-brittle.
- FAD allows to obtain simple Limit Load Diagrams for determining acceptable flaws.

GRAPHICAL ABSTRACT

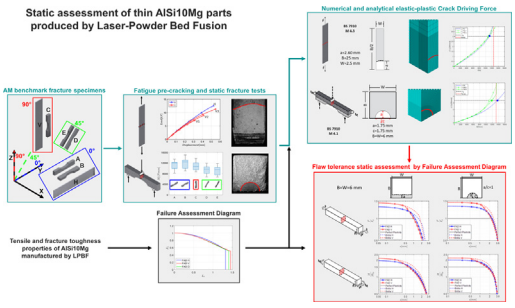

ARTICLE INFO

Article history:
Received 10 June 2022
Revised 1 October 2022
Accepted 20 October 2022
Available online 27 October 2022

Keywords:
Laser Powder Bed Fusion
AlSi10Mg
Fracture toughness
Mechanical properties
Failure Assessment Diagram
Building orientation

ABSTRACT

Several factors must be considered within the assessment of parts produced by Additive Manufacturing (AM) such as, for example, heterogeneous microstructure, process-induced defects, surface quality, residual stresses, and dependence on the material's properties with the building orientation. All these factors severely affect the resistance to static and fatigue loadings of AMed components. Among the possible failure mechanisms, the failure promoted by static loadings when cracks are present is one of the most important failure conditions, in particular for the as-built parts, which might have reduced fracture toughness and ductility compared to the wrought alloy counterpart. In this work, we present a comprehensive approach to the static assessment of AlSi10Mg parts manufactured by Laser Powder Bed Fusion. Two benchmark fracture geometries were designed to investigate the typical AM geometrical features: i) thin walls in tension and ii) notched components in bending. Finite Element analyses of the benchmark specimens showed that an approach based on elastic–plastic fracture mechanics parameters is needed to correctly predict the experimental failures, despite the quasi-brittle behaviour shown by the AlSi10Mg alloy. In view of these results, this paper explores the applicability of the Failure Assessment Diagram (FAD), a tool used for conventional ductile materials, to static assessment of AMed parts. The results show that the assessment approach based on the FAD makes it possible to properly predict the experimental failures of the benchmark specimens.

1. Introduction

In the last decade, Additive Manufacturing (AM) has been experiencing an ever-growing industrial application [1], in particular for the medical [2], automotive [3] and aerospace sectors [4–6]. Concurrently, the exploitation of AM's extraordinary potential requires new and reliable product design strategies, and this is challenging for engineers and researchers even in well consolidated industrial sectors. The mechanical properties of the finished products depend on the starting material as much as they do on the AM production parameters, way more than for traditional tech-

* Corresponding author.
E-mail address: stefano.beretta@polimi.it (S. Beretta).

https://doi.org/10.1016/j.matdes.2022.111292

Nomenclature

Abbreviations

AM	Additive Manufacturing
L-PBF	Laser Powder Bed Fusion
FAD	Failure Assessment Diagram
FE	Finite Element
CDF	Crack Driving Force
SIF	Stress Intensity Factor
3 PB	Three-point bending
CT	Compact Tension
LLD	Limit Load Diagram

Symbols

P	Laser beam power
h	Hatch distance
v	Scan speed
t	Layer thickness
B	Specimen thickness
W	Specimen width
L	Specimen length
H	Specimen height
r	Notch radius of 3 PB specimens
R	Load ratio
n	Ramberg–Osgood exponent
R_m	Ultimate Tensile Stress
$R_{p,0.2\%}$	Yield Strength corresponding to 0.2% plastic strain
E	Young modulus
ν	Poisson's ratio
α	Crack depth to component's width ratio
ε_f	Failure strain
σ	Engineering stress
σ_{flow}	Flow stress
ε	Engineering strain
J_Q	Material fracture toughness expressed in terms of J-integral, to be qualified
J_{IC}	Critical material fracture toughness expressed in terms of J-integral
J_{mat}	Material fracture toughness expressed in terms of J-integral
K_{IC}	Critical material fracture toughness expressed in terms of SIF
K_{mat}	Material fracture toughness expressed in terms of SIF
K_{max}	Maximum SIF at the end of the pre-cracking phase
ΔK	SIF range
K	SIF
Δa	Crack advancement
F_f	Experimental failure tensile load
$F_{FE,K}$	Failure tensile load predicted by FE analysis using liner-elastic material properties
$F_{FE,J_{mat}}$	Failure tensile load predicted by FE analysis using elastic–plastic material properties and J_{mat} as limit condition
$F_{FE,R-curve}$	Failure tensile load predicted by FE analysis using elastic–plastic material properties and material R-curve
M_f	Experimental failure bending moment
$M_{FE,K}$	Failure bending moment predicted by FE analysis using linear-elastic material properties
$M_{FE,J_{mat}}$	Failure bending moment predicted by FE analysis using elastic–plastic material properties and J_{mat} as limit condition
$\sqrt{J}$	Square root of the J-integral
$\sqrt{J_{mat}}$	Square root of material fracture toughness expressed in terms of J-integral
$\sqrt{J_{FE}}$	Square root of the J-integral obtained as output of FE analysis using elastic–plastic material properties
$\sqrt{J_{el}}$	Square root of the J-integral obtained as output of FE analysis using linear-elastic material properties
Y	Boundary correction factor
a	Crack depth or length
$a\prime$	Lesser crack depth for "Double" cracks
c	Crack half-width considering semi-elliptical geometry for "Semi", "Corner" and "Hybrid" cracks
$c\prime$	Lesser crack half-width for "Double" cracks
d	Distance between crack deepest point and nearest edge
e	Minimum distance between two cracks ("Double")
a_n	Notch depth
S	Nominal tensile stress
F	Tensile load
F_{pc}	Local plastic collapse tensile load
M_{pc}	Bending moment of local plastic collapse
F_y	First-yield tensile load
M_{Ip}	First-yield bending moment
A_{net}	Ligament area
A_c	Portion of ligament area in compression
A_t	Portion of ligament area in tension
y_c	Centre of gravity of the portion of ligament area in compression
y_t	Centre of gravity of the portion of ligament area in tension
F_{FAD}	Failure tensile load predicted by analytical calculations with FAD and/or CDF
M_{FAD}	Failure bending moment predicted by analytical calculations with FAD and/or CDF
L_r	Ligament yielding
K_r	Ratio between SIF and K_{mat}
$\overline{L}_r$	Ligament yielding of the assessment point
K_r	Ratio between SIF and K_{mat}
$\overline{K}_r$	Ratio between SIF and K_{mat} of the assessment point
Z	Plastic section modulus
FS_U	Factor of safety on ultimate load
FS_Y	Factor of safety on yield load
a_p	Maximum acceptable defect corresponding to the design load
a_f	Final physical crack length
a_0	Initial physical crack length
b_0	Ligament length before the fracture toughness test
V	Correction factor of SIF for secondary stresses
R_v	Surface roughness parameter related to maximum valley of profile
R_t	Surface roughness parameter related to total height of profile
$\sigma_{res,100\mu m}$	Residual stress measured at a depth of 100 μm
K_t	Stress concentration factor of 3 PB specimens
K_J	Elastic–plastic equivalent SIF
β	Strucutral constraint factor
β_T	Strucutral constraint factor from T-stress
α	Material fitting parameter for K^c_{mat}
k	Material fitting parameter for K^c_{mat}
K^c_{mat}	Constraint-dependent material fracture toughness expressed in terms of SIF
J^c_{mat}	Constraint-dependent material fracture toughness expressed in terms of J-integral
T	Linear- elastic triaxiality parameter T-stress

nologies [7]. New material features and characteristics such as microstructure, type of defects, surface quality, and residual stresses, obtained with AM might be significantly different from those obtained from traditional processes. These differences necessarily determine a change of *ratio* in the design procedures which have to consider the new material signatures introduced by the AM processes.

Currently, metal AM, and in particular Laser Powder Bed Fusion (L-PBF), has achieved high quality standards of the fabricated parts, especially for some classes of alloys, such as, for example, Al-based ones. Nevertheless, there remain several critical features that have to be considered in static and fatigue assessments, in particular: i) the inherent presence of defects [8,9], ii) the residual stresses [10], iii) the influence of the microstructure [11], and iv) poor surface finishing [12]. On top of these factors, the building orientation determines anisotropic material properties. In details, the main types of volumetric/internal defects that characterize the 3D printed Al alloys are [13,14]: i) irregular unmelted powder particles (lack of fusions), ii) gas pores; iii) keyhole type pores located at the base of melt pools; iv) laser spatter. Formation mechanisms of these anomalies and their detection have particular interest because of the possibility of manufacturing and post-process strategies capable of mitigating defect formation [15].

While the influence of these factors on the fatigue performance of L-PBF parts has been covered by several studies [12,8–10,16–19], less attention was devoted to systematic analyses of the static failures. The unstable failure of flawed parts is particularly important for those components that are mainly designed for static loads, as is the case of space components [20]. A proper definition of a fracture-based static assessment that accounts for the characteristics of as-built L-PBF products is therefore of the utmost importance, especially for materials that could be classified as 'brittle', due to their low ductility.

The AlSi10Mg alloy selected in this paper is characterised by a consolidated database and knowledge of L-PBF printing parameters which yield very low porosity and defects [12]. Several works have already reported how the mechanical properties of the L-PBFed AlSi10Mg parts are significantly affected by the micro and meso-structures induced by the manufacturing process. We note that some of the mechanical properties of this AlSi10Mg alloy in the as-built condition are better than those for wrought and cast items [7,21–23]. On the micro-scale, grain refinement is observed, due to the rapid cooling which imparts enhanced strength and relatively low ductility (between 5% and 10%) [7]. In particular, the tensile behaviour is characterised by an increased yield strength compared to the wrought counterpart and a ratio $R_m/R_{p,0.2\%}$ that can reach up to approximately 2 [11,23,24]. On a larger scale, the layer-by-layer melting strategy determines a meso-structure which induces the well-known anisotropy of the mechanical properties [25,26]. The L-PBF AlSi10Mg alloy can then be considered a *quasi-brittle* material [27] that is charaterised by anysotropic mechanical behavior. These material properties severely affect the tolerance to flaws/defects of AMed parts and are required to be properly considered for a reliable design.

For brittle materials and ductile materials with applied stress below 1/3 of yield strength, the static assessment of flawed parts can be performed adopting the linear elastic fracture mechanics theory and the Stress Intensity Factor (SIF) as the Crack Driving Force (CDF) parameter [28]. SIFs solutions can be found in compendia [29–32], or they can be calculated by dedicated Finite Element (FE) analyses. On the other hand, the static assessment of ductile materials with higher stresses requires the elastic–plastic principles and hence the adoption of different CDF parameters, i.e. the J-integral. In general, analyses based on the J-integral are rather complex and simplified approaches should be considered. For this reason, in the 1970s, procedures based on the so-called Failure Assessment Diagram (FAD) were developed for power generating applications [33]. The FAD procedure provides an analytical framework for accounting for plasticity-induced failures by proper corrections of simple linear-elastic solutions. Remarkably, the FAD found affirmed industrial application [34] and it is nowadays formalised by standards adopted in different sectors, such as the aerospace, civil, offshore and chemical ones [35,36], especially considering welds [37], where flaws/defects related to manufacturing process occur as for the AM processes [38,39].

It is therefore essential for the AM industry to introduce assessment routes and establish quality control tools for the acceptance of critical defects that could lead to failure [40]. In the scenario of new standards requiring the definition of *critical defect size* [41], this paper aims to provide a comprehensive approach for the static assessment of AMed parts made of a *quasi-brittle* (or *low-ductility*) material such as AlSi10Mg.

Accordingly, we adopted two benchmark fracture specimen geometries that were designed to investigate the effect of tensile and bending stresses on thin walled AMed parts accounting for the typical signature of the AM process represented by the material's anisotropy. The benchmark specimens were printed in three different orientations, 0°, 45° and 90°, alongside tensile and fracture toughness standard specimens for material characterisation. Linear-elastic and elastic–plastic FE analyses of benchmark specimens were performed to study the type of failure and evaluate what is the expression of the driving force (elastic or elasto-plastic) able to describe the experiments. Eventually, the applicability of the FAD considering the material properties obtained was then investigated.

The structure of this paper is as follows: Section 2 describes the specimen geometries and the experimental setup, Section 3 reports the results of the benchmark specimens' static fracture tests. The FE analyses performed on selected benchmark specimens are reported in Section 4, while Section 5 introduces the FAD procedure and shows its application to the same selected benchmark specimens. Section 6 provides a critical discussion on the application of the FAD to all benchmark specimens and an exemplary use of the FAD as a flaw tolerance tool is shown in Section 7. Finally, conclusions are summarised in Section 8.

2. Experimental campaign planning

2.1. Manufacturing of specimens

AlSi10Mg specimens were manufactured using an SLM 280HL v1.0 system equipped with two 400 W Yttrium fibre lasers working in parallel in a build chamber that measures 280x280x350 mm^3 (SLM Solution Group AG). The build chamber was flooded with argon to reach oxygen levels lower than 0.2% during the printing process. The printing parameters were as follows: beam power P = 350 W, hatch distance h = 0.13 mm and scan speed v = 1650 mm/s. The selected layer thickness was t = 50 μm and produced an energy density of 32.63 J/mm^3. The building platform was pre-heated up to 150°C. The scan strategy adopted stripes rotated by 67° after each layer and the scanning order was two contours and then perform the hatch scanning. AlSi10Mg powder, produced by ECKA Granules, was characterized by a mean granule size of 37 μm, D_{10}=21 μm and D_{90}=65 μm with a flowability of 80 s/50 g. All the manufactured specimens did not undergo any post-processing operation (e.g. stress relief, heat treatments) and they were tested in the 'as-built' condition. The specimens' relative density was 99.1%, measured according to ASTM B692 [42].

2.2. Benchmark fracture specimens

The experimental campaign aimed to perform static fracture tests on typical AM geometries. We adopted two benchmark specimens, as depicted in Fig. 1(a, b), printed in two Batches. The first geometry represents the typical AM feature of thin sections, a simple rectangular plate of width W = 25 mm and thickness B = 2.5 mm that was manufactured according to two orientations (Fig. 1(b)). The horizontal (H) orientation was determined with the loading axis to be parallel to the building platform (angle 0°), while for the vertical (V) orientation the loading axis was perpendicular to the building platform (90°). The specimens, hereafter referred to as thin plates, were printed within Batch 1.

A thicker specimen (B = 6 mm) characterised the second benchmark geometry. In this case, a notched three-point bending (3 PB) specimen was employed. The nominal length was L = 60 mm and the nominal height H = 10 mm. The notch of the 3 PB specimens was defined as a cylindrical surface with radius of r = 20 mm at the mid-span of the specimen's length. The cross section corresponding to the maximum notch depth was a square with nominal sides of 6 mm. The 3 PB specimens were manufactured in Batch 2 according to three orientations (0°, 45°, 90°) and two additional variants according to tilt angles for the horizontal and diagonal orientations [12]. In particular, the A and B orientations (Fig. 1(b)) were characterised by a bending stress parallel with the building platform. The difference between A and B was a tilt of 90° around the longitudinal axis of the specimens. The C orientation allowed a bending stress perpendicular to the building platform, while the D and E orientations were defined by an inclination of 135° and 45°, respectively (see also Table 1). All tests on the benchmark specimens were performed at room temperature, in air.

2.2.1. Thin plates

Before the tests, the thin plates were machined via Electron Discharge Machining to produce a lateral notch with nominal depths ranging from 500 μm to 2.5 mm, acting as a crack starter. Different notch lengths were studied to induce a purely fracture toughness-dominated failure (longer notches) or a failure which could be characterised by large plasticity in the non-cracked ligament (short notches). The lateral surfaces were successively polished by means of sandpaper with increasing grit from 360 to 800, to observe the crack length during the subsequent pre-cracking phase. The pre-cracking was performed on an MTS 370 Landmark equipped with a 25 kN load cell, using cyclic loading in tension. The crack length a at the end of pre-cracking was measured by means of an optical microscope to calculate the final maximum applied SIF K_{max} which was 11 MPa$\sqrt{m}$ for the H orientation and 6.5 MPa$\sqrt{m}$ for the V orientation. The SIF was calculated with formulations by [43].

The fracture tests were carried out in displacement control. The maximum load reached by each specimen was registered by the test machine as the failure load F_f. The fracture surfaces were then analysed by means of an optical microscope to measure the notch length and the crack lengths before and after the fracture tests. Values of width W, thickness B, notch length a_n and total pre-crack length a are shown in Table 2 for each specimen.

2.2.2. Three-point bending specimens

The 3 PB specimens were part of a test campaign for determining the effect of the printing orientation on the fatigue properties of this AlSi10Mg alloy (for further details see [12]). The 3 PB specimens had been subjected to fatigue cycles at load ratio R = 0.1 under a three-point bending configuration. This procedure allowed the nucleation and propagation of fractures without any crack starter. The tests were stopped at 10% decrease in the specimen stiffness. Within this research activity, the specimens were tested using an Instron 10000 machine to determine the maximum load for fracture. The tests were conducted in displacement control with a cross-head speed of 1.5 mm/min and the load–displacement curves were recorded. Successively, the fracture surfaces were analysed with a scanning electron microscope (Zeiss SEM model EVO 50) to obtain the geometry and dimensions of the cracks. In

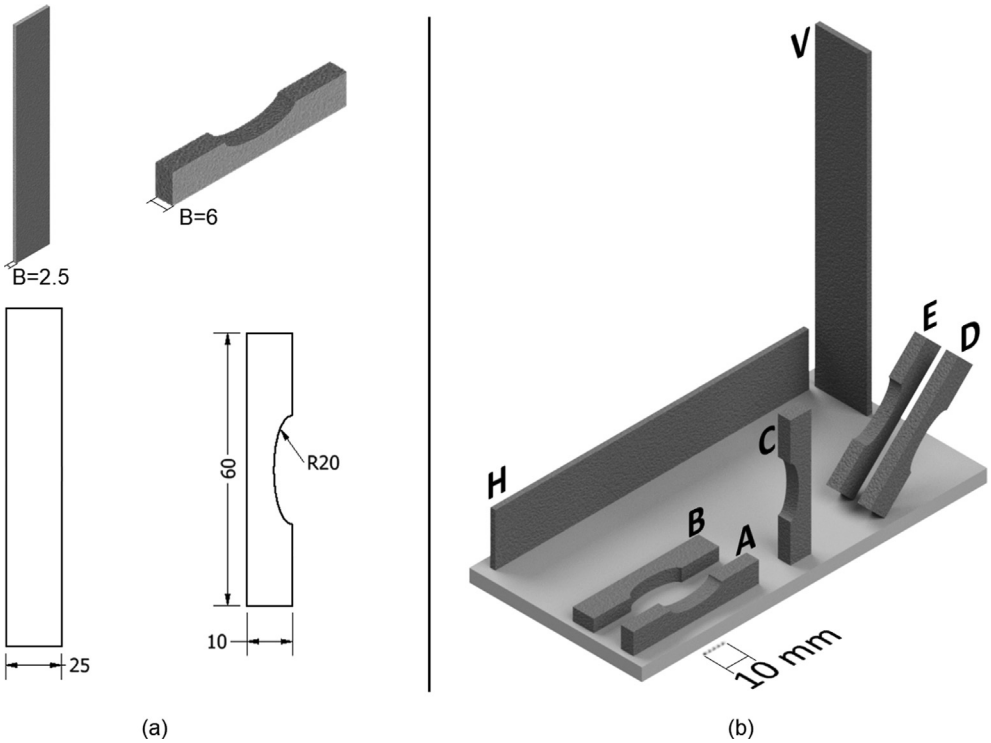

Fig. 1. Benchmark specimens adopted in this study: (a) thin plate and notched three-point bending geometries; (b) overview of the building layout.

Table 1
Experimental planning for the benchmark specimens.

Type of specimen	Orientation	Batch	Number of tests	Total
Thin plate	H (0°)	Batch 1	3	
(Fig. 1(b))	V (90°)		3	6
3 PB	A (0°)	Batch 2	7	
(Fig. 1(b))	B (0° side)		8	
	C (90°)		7	
	D (135°)		5	
	E (45°)		8	35

Table 2
Width W, thickness B, notch length a_n and total pre-crack length a for the thin plates.

Specimen	W[mm]	B[mm]	a_n [mm]	a [mm]
H	25.26	2.37	0.82	2.60
V1	25.10	2.40	2.71	3.52
V2	25.10	2.40	1.43	2.53
V3	25.10	2.34	0.48	1.32

addition, the longitudinal position of the failure location was measured by means of a 2 Megapixel Allied Vision Manta CCD camera, equipped with a lens system produced by Navitar. This made it possible to precisely calculate the failure bending moment M_f at the cracked section.

Tables 3 and 4 summarize the measurements of surface roughness and residual stresses performed on the 3 PB specimens, extensively reported in Beretta et al. [12].

2.3. Material properties

This AlSi10Mg alloy was characterised via standard specimens in terms of tensile behaviour and fracture toughness properties in air at room temperature. The selected specimens geometries were cylindrical [44] and Compact Tension (CT) [45], respectively. Three orientations for each specimen geometry were investigated (0°, 45°, 90°). Details on the specimens geometries, orientations and testing procedures can be found in A. The monotonic properties are reported in Table 5. In particular, the table shows the elastic modulus E, the yield strength $R_{p,0.2\%}$, the ultimate tensile stress R_m, the strain at failure ε_f and strain hardening exponent n. The strain hardening exponent n was obtained by a least-squares fitting of the Ramberg–Osgood equation [27]:

$$\varepsilon = \frac{\sigma}{E} + 0.002\left(\frac{\sigma}{R_{p,0.2\%}}\right)^{1/n} \tag{1}$$

The monotonic properties were comparable with data from literature on the same AlSi10Mg alloy produced by L-PBF in the as-built condition [21–23,25,46–50].

The fracture toughness properties were obtained by adopting the single specimen resistance curve (R-curve) method. From the obtained R-curves, reported in A, J_{mat} values were computed as J_Q according to ASTM E1820 [45] and the equivalent K_{mat} was calculated as:

$$K_{mat} = \sqrt{\frac{E}{(1-\nu)^2} J_{mat}} \tag{2}$$

where Poisson's ratio ν was assumed equal to 0.3. The K_{mat} values were required for the implementation of the FAD procedure in Section 5 and are reported in Table 6 alongside the J_{mat} values. In accordance with the literature [11,49,51,52,50], this AlSi10Mg alloy shows significant anisotropy in terms of fracture toughness. The V orientation shows lower fracture toughness values compared to the H orientation, for both Batches 1 and 2 (-32% and −53%, respectively). This evidence is related to the different crack paths [53,49,51,50]: for specimens printed with an inclination of 0° (H) the layers are perpendicular to the crack plane while, for specimens printed with an inclination of 90° (V), the layers are parallel to the crack plane, and this provides a more favourable crack path which follows the melting pool boundaries. It is worth observing that the specimens printed in Batch 1 with an inclination of 45° (D) showed a fracture toughness with values corresponding to the lower bound of V specimens.

Considering that for Batch 1 V and D orientations showed similar behaviour, J_{mat} and K_{mat} of the V orientation for Batch 2 were used for the D orientation for Batch 2 as a reasonable approximation. Two studies on fracture toughness of AlSi10Mg produced by LBPF with orientations 0°, 45° and 90° showed a similar trend [51,52]. Both studies showed that the 45° orientation had intermediate values, close to the 90° orientation. These results support the choice of taking the fracture toughness of V orientation as the reference value for fracture analyses of the D and E orientation of 3 PB specimens.

Table 3
Comparison of roughness parameters for the 3 PB series (adapted from [12]).

Series	R_v [μm] $\mu \pm 2\sigma$	R_t [μm] $\mu \pm 2\sigma$
A	38.0±12.4	58.4±25.5
B	18.8±10.8	32.6±14.3
C	12.9±5.6	23.6±9.6
D	38.9±28.1	61.3±40.5
E	18.1±16.5	29.4±27.9

Table 4
Summary of residual stress measurements at a depth of 100 μm for the 3 PB series (adapted from [12]).

Series	$\sigma_{res,100\mu m}$ [MPa] $\mu \pm \sigma$
A	-6.9±10.3
B	-14.0±9.4
C	167.7±20.1
D	150.7±40.1
E	98.6±14.6

Table 5
Monotonic properties of this AlSi10Mg alloy.

Orientation	E [GPa]	$R_{p,0.2\%}$ [MPa]	R_m [MPa]	ε_f [%]	n
H (0°)	72.2±1.6	229±4	379±2	4.7±0.4	0.144
V (90°)	69.3±2.5	208±1	396±8	5.4±0.7	0.202
D (45°)	65.2±3.2	206±3	383±8	5.4±1.1	0.196

Table 6
Fracture toughness values of this AlSi10Mg alloy as J_{mat} and K_{mat} for each Batch and orientation.

Orientation	Fracture toughness			
	J_{mat}[N/mm]		K_{mat} [MPa$\sqrt{m}$]	
	Batch 1	Batch 2	Batch 1	Batch 2
H (0°)	9.1±0.2	11.2±0.1	26.9±0.3	30.0±0.4
V (90°)	4.3±0.6	7.6±0.4	18.0±1.2	24.6±0.9
D (45°)	4.6	-	18.2	-

3. Experimental results

3.1. Thin plates

The experimental Load–Displacement diagrams for the thin plates extracted from the machine are depicted in Fig. 2, where it can be recognised a *brittle* behaviour with some degree of non-linearity. Values of crack length to width ratio α=a/W and experimental failure loads F_f are reported in Table 7. It is interesting to note that the failure loads F_f of specimen H and V2 are significantly different, despite having similar α, which can be related to fracture toughness anisotropy.

3.2. Three-point bending specimens

All the tests showed *load-stroke* curves with a non-linear *brittle* failure behaviour, similar to the ones in Fig. 2: they are here analysed only in terms of the maximum bending moment reached during the tests. Fig. 3 shows the box plots of the failure bending moments of the 3 PB specimens. Orientations A and B show the highest values of failure loads in accordance with the highest fracture toughness measured on the H CT specimens. On the other hand, orientation E shows the lowest average failure bending moment and this further confirms the trend of the fracture toughness values.

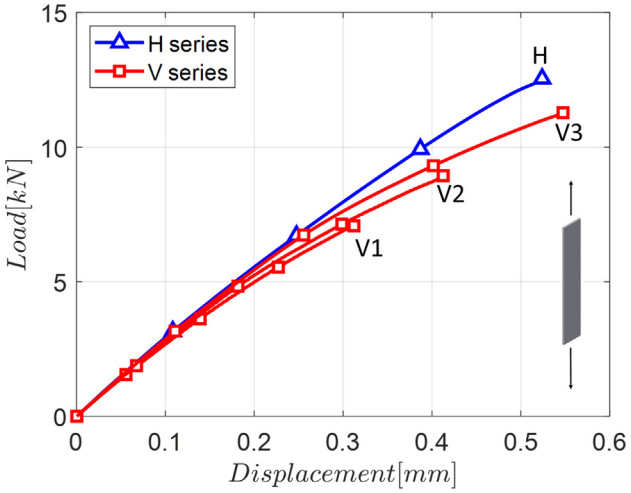

Fig. 2. Experimental Load–Displacement diagrams of the thin plates.

Table 7
Crack length to width ratio α and experimental failure loads F_f of the thin plates.

Specimen	α	F_f [N]
H	0.10	12543
V1	0.14	8070
V2	0.10	8949
V3	0.05	11278

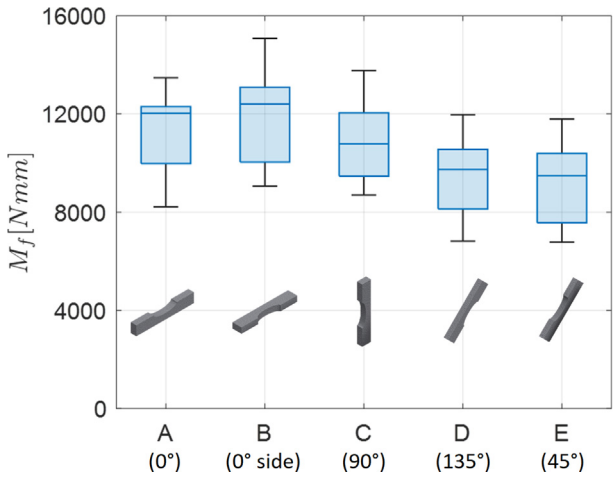

Fig. 3. Experimental failure bending moments of the 3 PB specimens.

The fatigue tests produced a plethora of crack geometries, each differing in position, aspect ratio and dimensions, as shown in Fig. 4. The crack depths ranged from 1.22 mm to 2.76 mm. Crack dimensions and failure bending moments M_f are reported in Tables B.1, B.2, B.3, B.4 in B.

4. FE analyses

The static failures of both thin plates and 3 PB specimens were studied with the FE modelling technique to investigate the crack driving force (CDF) parameter of the benchmark specimens. As will be shown below, FE simulations based on the calculation of the J-integral were computed for selected specimen and crack geometries using Simulia Abaqus by Dassault Systèmes. The failure condition was analysed comparing the CDF with the fracture toughness J_{mat} measured for the specific orientation and batch.

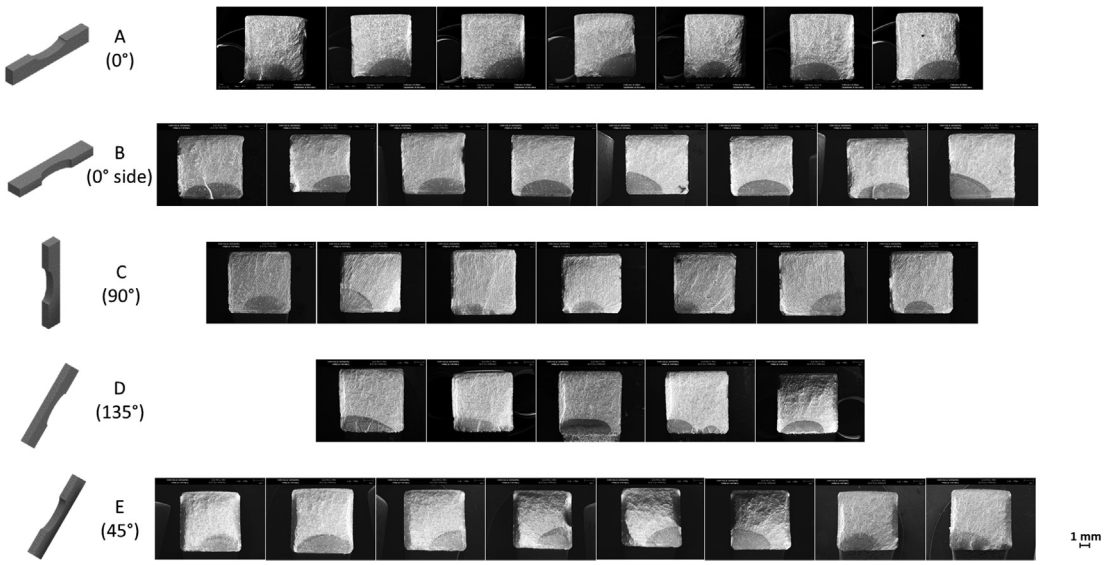

Fig. 4. Fracture surfaces of the 3 PB specimens.

The Von Mises yield surface was employed for the numerical analyses [27].

4.1. FE - Thin plates

FE models of the thin plates were developed using the crack plane xy (Fig. 5(b)) as the plane of symmetry. The crack surfaces obtained with the optical microscope allowed us to properly reproduce the crack front shape on the model (Fig. 5(c)). The symmetry condition was then applied on the crack plane. The simulation was performed with 8-node linear brick elements with reduced integration (C3D8R). The dimension of the elements was set to approximately 100 μm in the region near the crack tip (Fig. 5(d)). The mesh size was defined after evaluating convergence of J-integral with a more refined mesh of 50 μm. The calibration of the material model considered the extrapolation of the true stress–strain curves beyond the experimental failure strain (Fig. 5(a)) by means of the Ramberg–Osgood Eq. (1). The FE simulations were performed by applying a remote incremental displacement to a reference point which was kinematically coupled with the top surface (Fig. 5(b)). As output, the axial reaction force was considered together with the J-integral values for different contours along the crack front. Convergence of J-integral values was obtained for contour numbers higher than 10. The elastic modulus and the Poisson's ratio were set to E = 70000 MPa and ν=0.3, respectively. In Fig. 6, we defined the CDF extracted at the deepest point of the crack (indicated by a red dot) as the square root of the J-integral $\sqrt{J}$ for a better comparison between linear-elastic (dashed blue line) and elastic–plastic (solid blue line) material properties. The deepest point was selected being the critical one for the thin plates. In fact, the J-integral varies through the thickness and the highest value was always found to be for the deepest point of the crack front. The average fracture toughness for Batch 1, in terms of $\sqrt{J_{mat}}$, is represented as a horizontal dashed black line, while the experimental failure load as a vertical dashed red line. The failure load estimated from the FE model was obtained as the intersection between the fracture toughness $\sqrt{J_{mat}}$ and the increasing $\sqrt{J}$.

Fig. 6(a, b, c, d) indicates that the adoption of a simple linear-elastic model would systematically overestimate the failure load. On the other hand, the elastic–plastic model predicts a failure load that is generally in good accordance with the experimental one.

The approach based on the comparison between $\sqrt{J}$ and $\sqrt{J_{mat}}$ does not consider that ductile and quasi-ductile metallic materials do not fail when $\sqrt{J} = \sqrt{J_{mat}}$, while they can further accommodate increments of loadings. This concept is contained in the so-called static resistance curve (R-curve) which is derived from the fracture toughness tests as the J-integral versus crack advancement Δa plot. The R-curves for the H and V orientations are reported in Fig. 7 by purple lines. The assessment based on the R-curve requires the definition of the parametric CDF curves (J-Δa) for different load levels. Then, additional FE models were implemented with increased crack sizes corresponding to crack extensions equal to 0.5 mm and 1 mm. Fig. 7(a, b, c, d) shows the CDF curves obtained for three different stress levels alongside the R-curves. For all the plots, the blue curves indicate a load level for which the crack is subjected to an initial crack advancement as the CDF curve is above the R-curve. However, the crack cannot further extend as the R-curve is higher than the CDF, that is, the material is capable to statically resist further crack advancements. On the other side, the orange lines and dots represent nominal stress levels just above the tangency condition between CDF and R-curve. For this case, the applied load is sufficiently high to determine the condition of unstable crack advancement, which is seen with the CDF curves always being above the corresponding R-curves. Therefore, the stress levels corresponding to the point of tangency were considered as those leading to unstable crack propagation and were used to compute the failure loads.

Table 8 shows a comparison between the experimental failure load F_f, the failure load predicted from the linear-elastic FE model $F_{FE,K}$, the failure load predicted with the elastic–plastic model $F_{FE,J_{mat}}$ and the failure load predicted with the R-curve $F_{FE,R-curve}$. The predictions performed with the elastic–plastic FE analyses, both that based on the fracture toughness J_{mat} and the one based on the R-curve, provide estimations close to the experimental values. The FE analyses performed with the linear-elastic FE model, instead, systematically over-estimate the failure load. This observation is of fundamental importance as for this AlSi10Mg alloy the ε_f is approximately 5% for all the orientations investigated, hence it can be classified as brittle [27], as many other Al-based alloys for AM [18]. This suggests that a simple approach based on the linear-elastic fracture mechanics could be sufficient to estimate the static strength of the benchmark specimens. However, as evidenced by the results presented in Table 8, the predictions

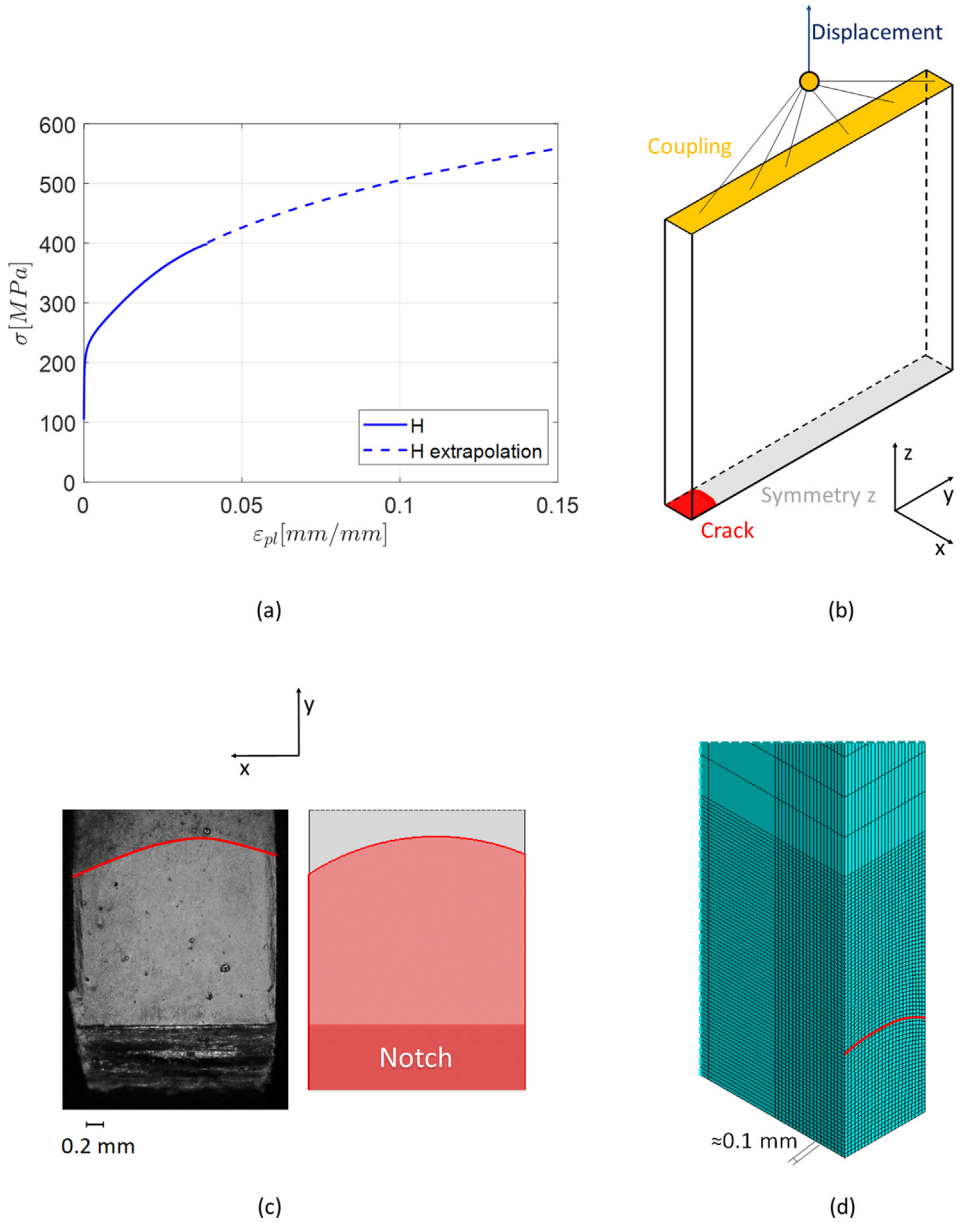

Fig. 5. FE model of the thin plate specimens showing: (a) the extrapolated tensile curve (dashed line); (b) loading and boundary conditions of the FE model; (c) physical crack and model crack; (d) a detail of the FE mesh near the crack front.

based on the linear-elastic fracture mechanics are strongly non-conservative. Therefore, concepts of elastic–plastic fracture mechanics have to be applied.

4.2. FE - Three-point bending specimens

Four 3 PB specimens were selected for FE analysis (Fig. 8). The crack shape was chosen to allow for direct comparison with the analytical results in Section 5.

The procedure adopted to model the selected 3 PB specimens was analogous to the one previously described for the thin plates. In this case, the crack plane yz (Fig. 9(a)) was the symmetry plane and, by considering the semi-elliptical cracks as centred on the fracture surface, the xz symmetry plane was exploited as well (Fig. 9b). Three-point bending conditions were reproduced by constraining the displacement in y direction of the topmost section of the crack surface, while a vertical displacement was applied incrementally to a reference point kinematically coupled with the nodes corresponding to the bottom roller (Fig. 9(a)).

The analysis performed on this global model was then used as the input for a sub-model analysis of a small region containing the crack surface. The sub-modelling allowed us to improve the accuracy of the J-integral calculations without significantly increasing the time needed for the analysis. The sub-model had a length of 2 mm and an element dimension of 70 μm in the region near the modelled crack front (Fig. 9(c)). Both model and sub-model simulations were performed with 8-node linear brick elements with reduced integration (C3D8R). Convergence of J-integral was evaluated using a mesh size of 50 μm for the sub-model. The material was the same as that described for the thin plates in Section 4.1. The outputs of the analyses were the vertical load and the J-integral calculated for different contours of the crack front (from the sub-model). J-integral results converged after contour number 6. The J-integral was evaluated for the deepest point of the crack front and the point on the surface: the one with higher

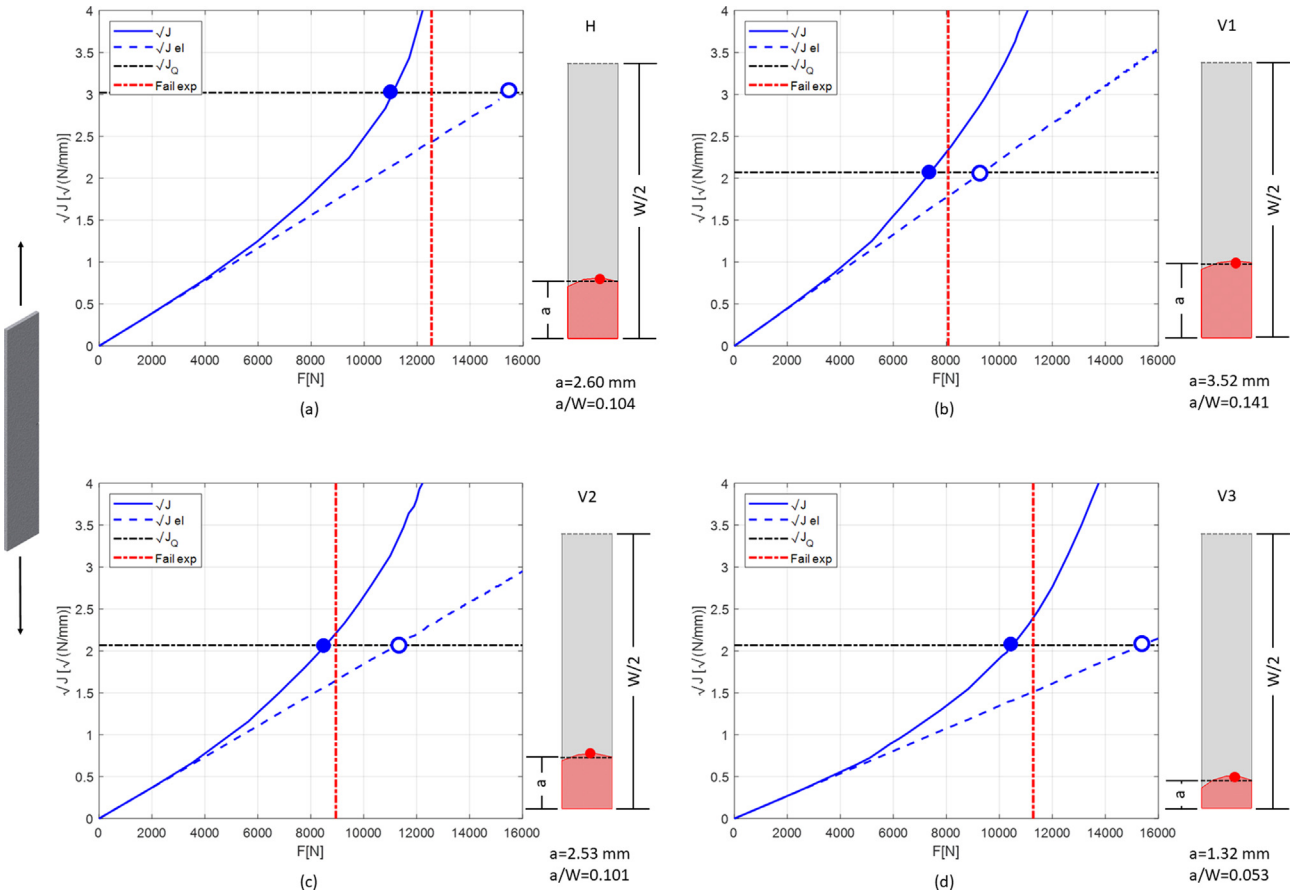

Fig. 6. CDF of thin plate specimens: (a) H; (b) V1; (c) V2; (d) V3. See the text for further details.

value was selected as the critical one for each specimen and is marked in Fig. 10 with a red dot.

Fig. 10 and Table 9 report the experimental failure bending moments M_f for all the modelled 3 PB specimens, alongside the failure bending moments predicted from the linear-elastic FE model $M_{FE,K}$ and the elastic–plastic model $M_{FE,J_{mat}}$. Analogously to thin plates, the failure load is overestimated using a simple linear-elastic model (Fig. 10(a, b, c, d)), while the elastic–plastic model predicts a failure load that is close to the experimental failure, although slightly non conservative for some cases (Fig. 10(a, b, c)), with a maximum error of 7%.

5. FAD analysis

In Section 4, we demonstrated that, given the material properties along a specific orientation, and designing a proper FE analysis which considers the elastic–plastic fracture mechanics parameter J-integral, it is possible to predict the failure load with good accuracy. However, an approach based on FE for the calculations of elastic–plastic parameters is complex and time consuming. For this reason, in this Section we extend and verify the adoption of the *Failure Assessment Diagram* (FAD) for AMed components. The key concept of FAD approach is that the elastic–plastic driving force ahead of a crack is approximated as [34]:

$$J = K^2/(E/(1-\nu^2)) \cdot f(L_r)^{-2} \tag{3}$$

where K refer to the SIF calculated for a given load F and $L_r = F/F_{pc}$; F_{pc} being the plastic collapse load of the section. The function $f(L_r)$ is lower than 1 for $F > 0.3 \cdot F_{pc}$ to take into account the increased driving force due to plastic strains ahead of the crack tip. [54]. The main steps of the FAD analysis given the crack shape, part geometry and applied load *F*, can be summarised as:

- Identification of a substitute geometry.
- Calculation of SIF *K* and plastic collapse load F_{pc} for the substitute geometry.
- Calculation of non-dimensional parameters $\overline{K}_r = K/K_{mat}$ and $\overline{L}_r = F/F_{pc}$.
- Component assessment: if the assessment point $(\overline{L}_r, \overline{K}_r)$ lies below the failure line in the L_rK_r plane, then the component design is considered safe, otherwise it is deemed potentially unsafe.

The FAD procedure typically described in standards [29–31] is defined as an "Option-based assessment" in which the Option number is correlated with the complexity of the analysis and the required material information. Using the nomenclature adopted by BS 7910, Option 1 requires knowledge of the yield strength, ultimate tensile stress and fracture toughness for the material, while Option 2 requires knowledge of the complete true stress–strain curve and fracture toughness. The reader is referred to C for a brief description of the analytical models of SIFs and yield loads used in this work and to Zerbst's book for a detailed and comprehensive definition of the FAD procedure [34].

In this work, Option 2 was selected for the analyses. Three failure lines, one for each orientation, were generated using the experimental true stress–strain curves obtained from the tensile cylindrical specimens described in A. The failure lines generated were used to compare the analytical elastic–plastic CDF with the CDF obtained from the FE analyses. The analytical elastic–plastic

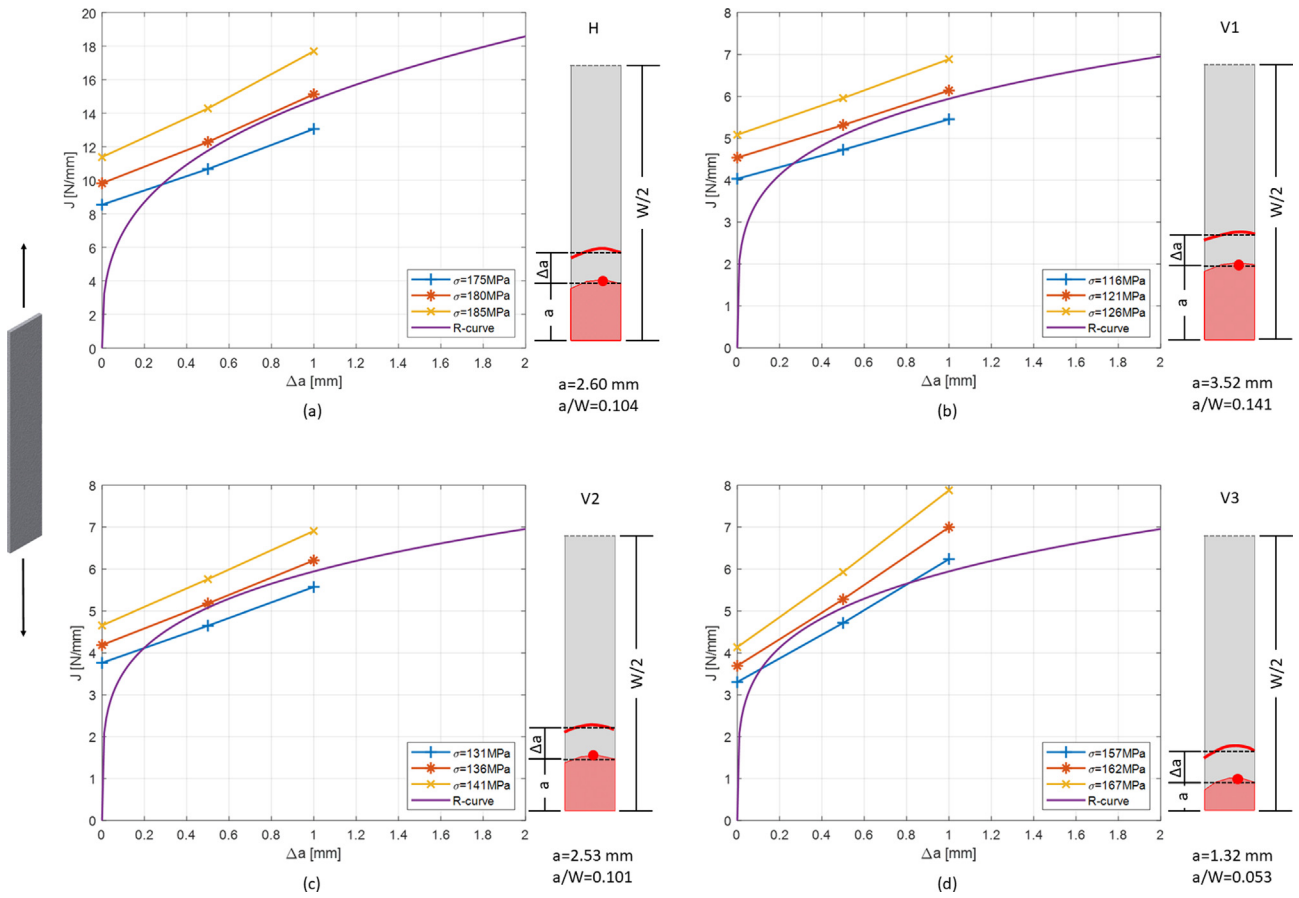

Fig. 7. R-curve vs CDF of thin plate specimens: (a) H; (b) V1; (c) V2; (d) V3.

Table 8
Experimental and predicted failure loads for the thin plate specimens.

	Experiments	Predictions		
Specimen	F_f [N]	$F_{FE,K}$ [N]	$F_{FE,J_{mat}}$ [N]	$F_{FE,R-curve}$ [N]
H	12543	15497	11063	11250
V1	8070	9267	7394	7563
V2	8949	11356	8555	8563
V3	11278	15342	10459	10187

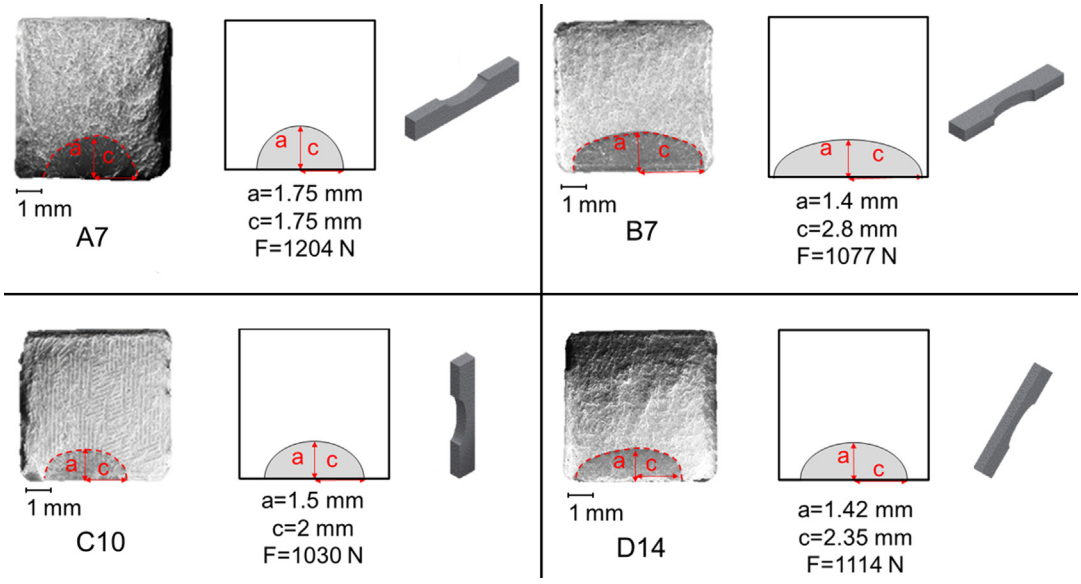

Fig. 8. Fracture surfaces, crack geometries and failure loads of the modelled 3 PB specimens.

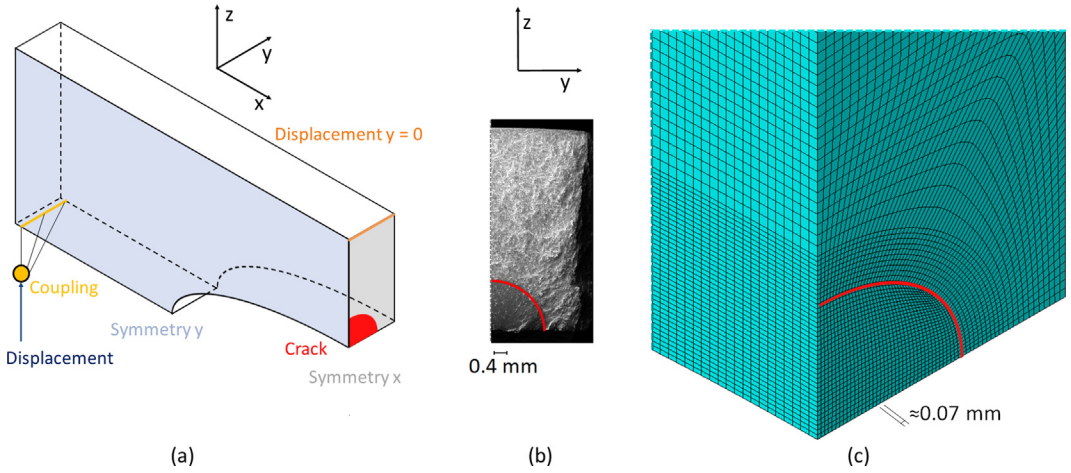

Fig. 9. FE model of the 3 PB specimens showing: (a) boundary conditions and imposed displacement, (b) fracture surface, (c) sub-model mesh.

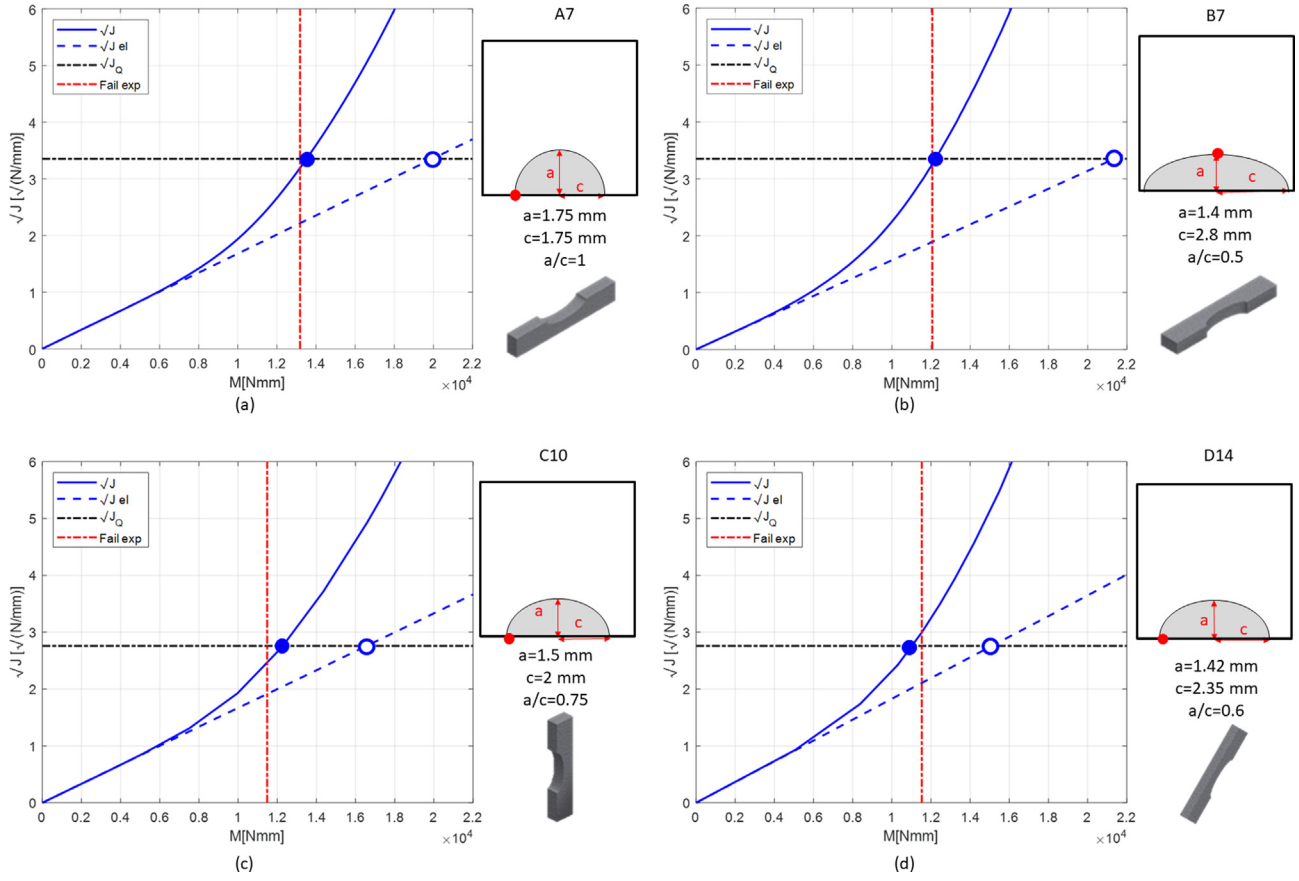

Fig. 10. CDF of 3 PB specimens: (a) A7; (b) B7; (c) C10; (d) D14.

Table 9
Experimental and predicted failure bending moments for the 3 PB specimens analysed.

	Experiments	Predictions	
Specimen	M_f [N·mm]	$M_{FE,K}$ [N·mm]	$M_{FE,J_{mat}}$ [N·mm]
A7	13184	19925	13512
B7	12062	21351	12225
C10	11485	16543	12271
D14	11530	15000	10985

CDF was calculated from the analytical SIF using Eq. 3. The analytical SIF of 3 PB specimens was always evaluated for the surface point of the crack front since it's the point of maximum for the SIF of the substitute geometry.

Substitute geometries for the analytical SIFs are reported in Fig. 11. For thin plates, the substitute geometry coincides with the specimens in terms of crack shape, component geometry and loading. The substitute geometry for 3 PB specimens only coincides in relation to crack shape, while the component's notched geometry under three-point bending was replaced by a bar square in sec-

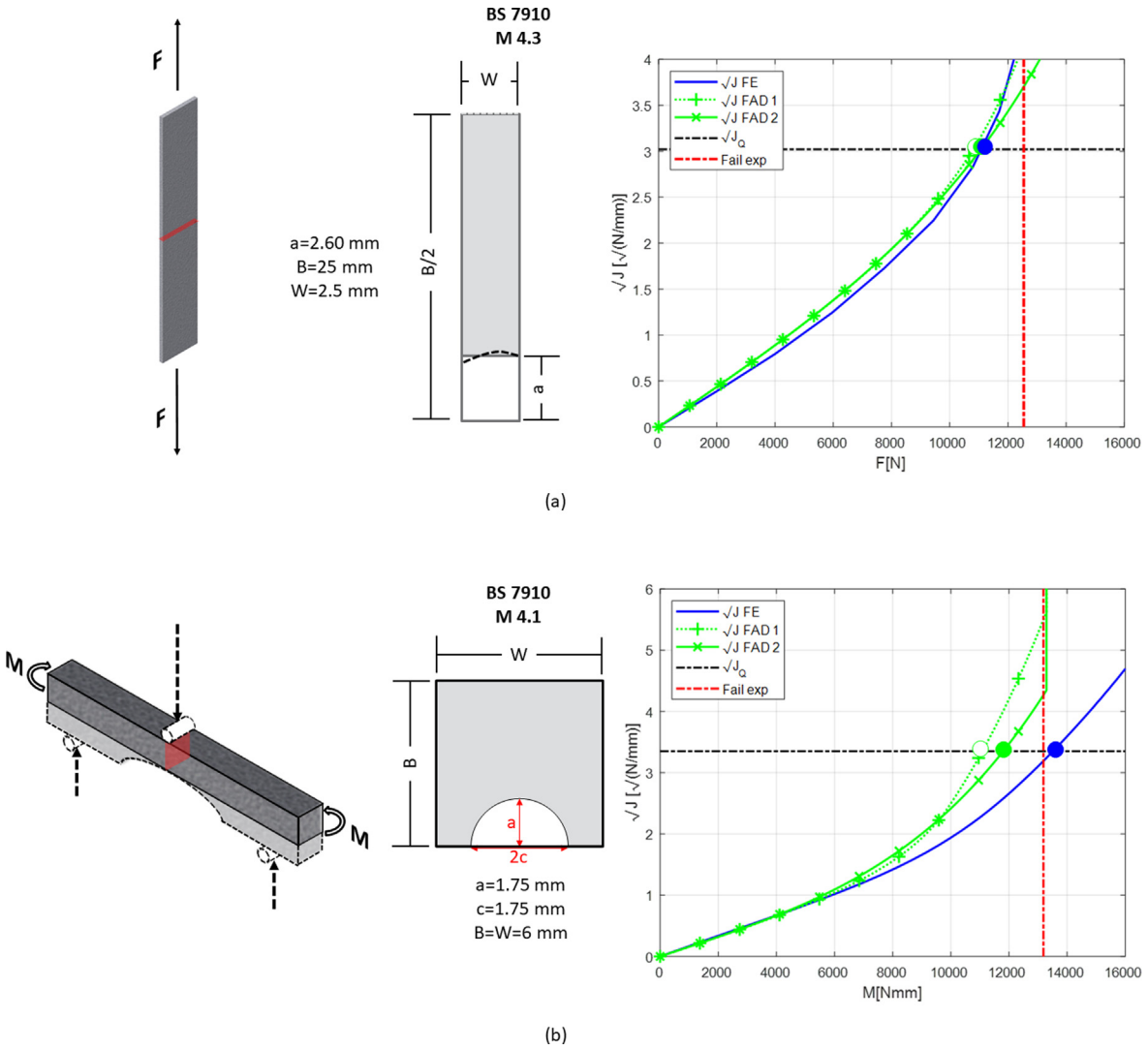

Fig. 11. Substitute geometry and loading type, crack shape and comparison between analytical and numerical CDF for: (a) thin plate specimen H and (b) 3 PB specimen A7.

tion under pure bending. This approximation is a good representation of the real geometry since the stress concentration factor for the notched section of the 3 PB specimens was negligible (K_t<1.05). The comparison of the CDF from FE with the CDF obtained analytically using the FAD's formulations shows the effect of the simplifications introduced by the use of substitute geometries. Fig. 11 displays the $\sqrt{J}$ versus applied load for the FE models as continuous blue lines and the values obtained with FAD Option 2 as continuous green lines. Only for this CDF analysis, the FAD Option 1 failure line for the H orientation was generated using the yield strength and strain hardening exponent of the true stress–strain curve. The $\sqrt{J}$ calculated using the FAD's failure lines displays a good agreement with the $\sqrt{J_{FE}}$ for the thin plate subjected to tension (Fig. 11(a)), while they yield conservative predictions for the case of the 3 PB specimen subjected to bending (Fig. 11(b)). This difference in prediction can be related to the aforementioned simplifications introduced by substitute geometries for the 3 PB specimens.

Subsequently, the experimental failures were investigated using the FAD (Fig. 12). The graph for thin plates shows the FAD for orientations H and V (Fig. 12(a)), while the graph for 3 PB specimens reports the FAD for orientation H, V and D (Fig. 12(b)). The assessment point for each specimen was generated considering both the experimental data and the FE analyses:

- $\overline{K}_r$ was calculated as the linear-elastic computational CDF that corresponds to the failure load divided by the fracture toughness.
- $\overline{L}_r$ was obtained as the experimental failure load divided by the local plastic collapse load.

For all the cases shown, the experimental failures are above the failure lines, providing a conservative prediction.

The FAD was also used to predict the failure loads of the benchmark specimens using the analytical SIF solutions. For each specimen, component geometry, loading type and crack dimensions were fixed, hence a linear increase of load resulted in a linear increase in both $\overline{L}_r$ and $\overline{K}_r$. All the load points that belong to a single specimen allowed us to draw a "specimen" line. The intersection of the "specimen" line with the relevant failure line identified the predicted failure point on the FAD. The predicted failure load was finally obtained by multiplying the $\overline{L}_r$ at the predicted failure point by the plastic collapse load of the benchmark specimen. For both thin plates and 3 PB specimens, the predicted failures (F_{FAD} and

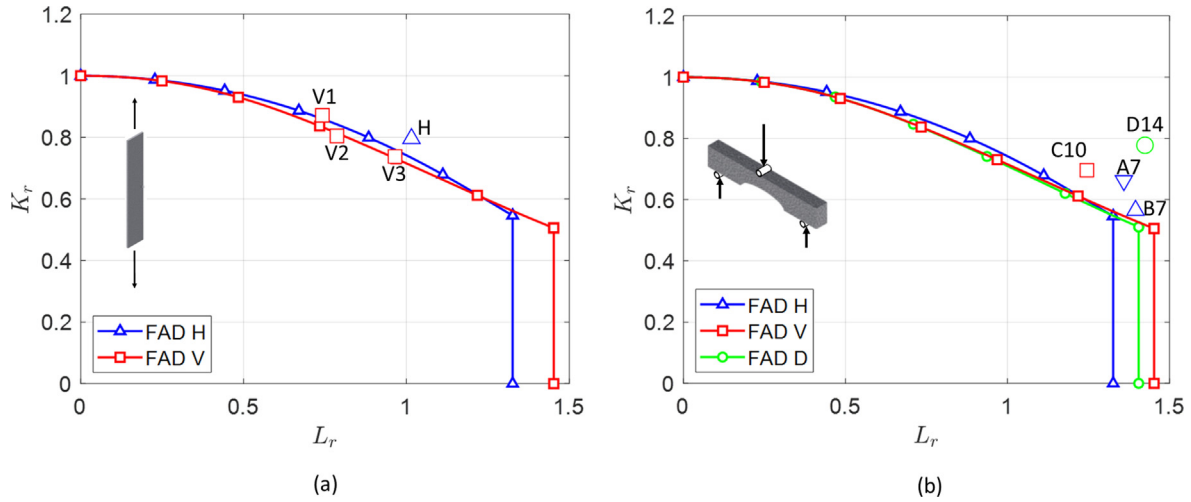

Fig. 12. FAD for: (a) thin plate specimens; (b) 3 PB specimens.

M_{FAD}) are in good agreement with the experimental failures, as can be seen in Tables 10 and 11. Residual stresses (RS) can be considered in the FAD as a secondary stress. In particular, the assessment point needs to be evaluated as:

$$K_r = K + V \cdot K_{RS} \tag{4}$$

where K is the SIF due to primary load, K_{RS} is the SIF due to RS and V is a weight factor. V is a function of L_r: it increases monotonically from 1 for $0<L_r<0.8$ and then decreases so that $V \ll 1$ for $L_r \to L_{r,max}$[34].

As for the presence of RS within the benchmark specimens (Table 4), residual stresses were measured on 3 PB specimens only to a depth of 400 μm. However, the fatigue cracks generated on 3 PB specimens were always much deeper than the measurement depth: consequently, we expect a significant stress relaxation of the RS. Moreover, L_r values for 3 PB specimens are always significantly above 1, which means that the contribution of RS would have a minor effect. Considering the combined effect of stress relaxation and high L_r, we decided to neglect the effect of RS on the analysis of 3 PB specimens.

Table 10
Experimental and predicted failure loads from FAD for the thin plate specimens.

	Experiments	Predictions
Specimen	F_f [N]	F_{FAD} [N]
H	12543	11078
V1	8070	7258
V2	8949	8610
V3	11278	10480

Table 11
Experimental and predicted failure bending moments from FAD for the 3 PB specimens analysed by means of FE.

	Experiments	Predictions
Specimen	M_f [N·mm]	M_{FAD} [N·mm]
A7	13184	11800
B7	12062	11830
C10	11485	11020
D14	11530	10500

6. Discussion of results

6.1. Effect of constraint on benchmark specimens

The standard specimens typically employed for the evaluation of fracture toughness K_{mat} are designed to have a high level of constraint at the crack tip (i.e. they are deeply cracked, with $a/W>0.5$) and thus define a lower-bound value, independent from size and geometry. [34,28] However, components usually are not so deeply cracked and hence have a much lower level of constraint. This leads to an increased resistance to crack propagation and thus to an increase in fracture toughness due to the constraint effect ($K^c_{mat}>K_{mat}$)[28,55]. The FAD procedure allows to take into account this effect by considering the following relationship between K^c_{mat} and K_{mat}, function of L_r and triaxiality parameter β [56]:

$$K^c_{mat} = \begin{cases} K_{mat} & \text{for } \beta L_r > 0 \\ K_{mat}\left[1 + \alpha \cdot (-\beta L_r)^k\right] & \text{for } \beta L_r \leqslant 0 \end{cases} \tag{5}$$

where α and k are material parameters, which can be obtained from experiments carried out on specimens with significantly different degree of constraint, while β is the structural constraint factor, which can be obtained from triaxiality parameters. In particular, considering T-stress $T, \beta_T = T/(L_r \cdot R_{p,0.2\%})$. When adopting a CDF analysis, the J^c_{mat} is directly obtained from Eqs. 2 and 5, while for the FAD, it's possible to modify the failure assessment line so that $K_r = f(L_r) \cdot K^c_{mat}/K_{mat}$ [34].

To investigate the effect of constraint on the benchmark specimens analyzed in Section 5, we evaluated the T-stress at failure for the critical point of each benchmark specimens. The T-stress was calculated using the same FE analyses described in Section 4, performed with linear elastic material properties.

Fig. 13 summarizes the effect of constraint for all the benchmark specimens investigated in Sections 4 and 5 and the standard compact tension (CT) specimens used for material characterization described in A. The vertical axis reports the values of K_J at failure normalized by the relevant K_{mat}, while the horizontal axis reports the T-stress at failure T divided by the relevant yield strength $R_{p,0.2\%}$. Positive values of $T/R_{p,0.2\%}$ represent high constraint conditions, typical of fracture toughness specimens, while negative values of $T/R_{p,0.2\%}$ represent low constraint conditions, typical of components. Standard CT specimens with $a/W \geqslant 0.5$ have a normalized T-stress $T = 0.6K/\sqrt{a}$ [34]. The single specimen value of material fracture toughness (K_{J_Q} in Table A.2 in A) was used for K_J.

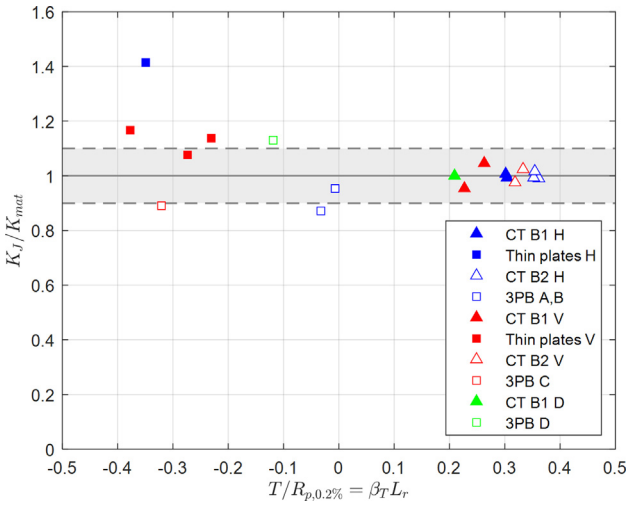

Fig. 13. Effect of constraint on fracture toughness of benchmark specimens.

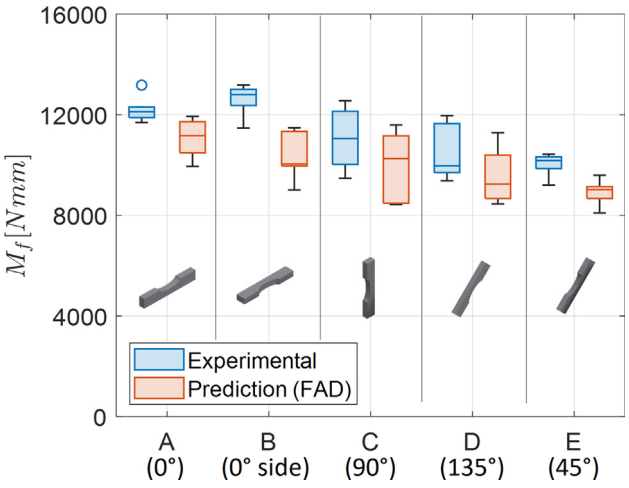

Fig. 14. Experimental and predicted failure bending moments from FAD of the 3 PB specimens.

Fig. 13 shows that for benchmark specimens $\beta_T L_r$<0: data shows a quite significant scatter and there is not a significant effect of constraint. Nevertheless, it can be also considered that the horizontal line K_J/K_{mat}=1 (together with a scatter band of ±10%) well describes the tendency of experimental fracture tests. Therefore we decided to neglect the effect of constraint, for the sake of conservatism and simplicity, in FAD analyses.

6.2. Failure Assessment of 3 PB specimens

In Sections 4 and 5, we provided a comprehensive analysis of the applicability of fracture mechanics elastic–plastic parameters to predict the static failure of cracked AMed parts. Figs. 6 and 10 show the analyses of failures for the thin plates and the 3 PB specimens performed by means of the J-integral parameter. For all the cases, providing i) the fracture toughness for the same orientation and batch and ii) the crack geometry, the approach based on the J-integral is observed to properly predict the failure load with excellent accuracy, especially for the thin plates in tension. On the other hand, despite the quasi-brittle behaviour of the present AlSi10Mg alloy, the linear elastic CDF parameter K yields to unconservative predictions. According to these results, the study explored the applicability of the FAD approach to statically assess cracked AMed parts. The application of the FAD methodology to AMed components is relevant, in particular for industrial applications where it is not feasible to perform complex elastic–plastic FE simulations.

Fig. 14 shows the experimental failures for the different orientations alongside the predicted failure from FAD, while the complete data on predicted failure bending moments is available in Tables B.1, B.2, B.3, B.4 in B. Re-characterisation of crack shapes is provided in C. Remarkably, failure bending moments estimated using the FAD are generally conservative, with a maximum error on the non-conservative side of 2%. It is interesting to see how the trend of predicted failures follows the trend shown by the experiments, in which the higher values of failure bending moments are attributed to orientations A and B, while the lowest one corresponds to orientation E. A relevant point is that the fracture toughness used for orientations A (0°) and B (0° on the side) was the same. However, fracture toughness in the literature obtained on specimen printed with 0° orientation on the side shows higher values than for the 0° orientation [26,53,52]. With higher values of material fracture toughness, the predicted failure bending moments would increase, thus obtaining results closer to the experimental failures.

7. Limit Load Diagram for AlSi10Mg and flaw tolerance

By considering only one combination of component geometry, crack shape and loading, it is possible to obtain a diagram displaying limit loads for different crack lengths. The diagram generated by representing the limit load associated to each crack length was called Limit Load Diagram (LLD). A simplified scheme for a flawed component under axial load is shown in Fig. 15. The first observation is that for a material with significant strain-hardening, as this AlSi10Mg, the collapse condition on the up-left side is higher than the limit condition $F/F_y = 1$ of a perfectly plastic material, because collapse is controlled by the *flow stress*. On the other hand, the down-right side of the LLD is controlled by the onset of fracture under the condition $J = J_{IC}$. Therefore, from the point of view of a static assessment, the limit line is valid for an *ultimate load* assessment. From a flaw tolerance perspective, the adoption of this LLD diagram for determining the *maximum acceptable defect* a_p for a given design load is hereafter described. In first instance, standards for AM components are the same as the ones for wrought components. Standards for space components by

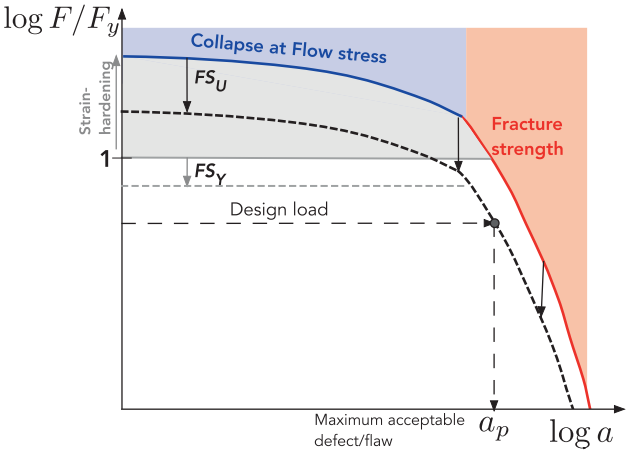

Fig. 15. Limit Load Diagram scheme with highlighted regions corresponding to plastic collapse at flow stress of the net section (blue), brittle fracture in presence of a crack (red), strain-hardening which allows for F/F_y values above 1 (grey).

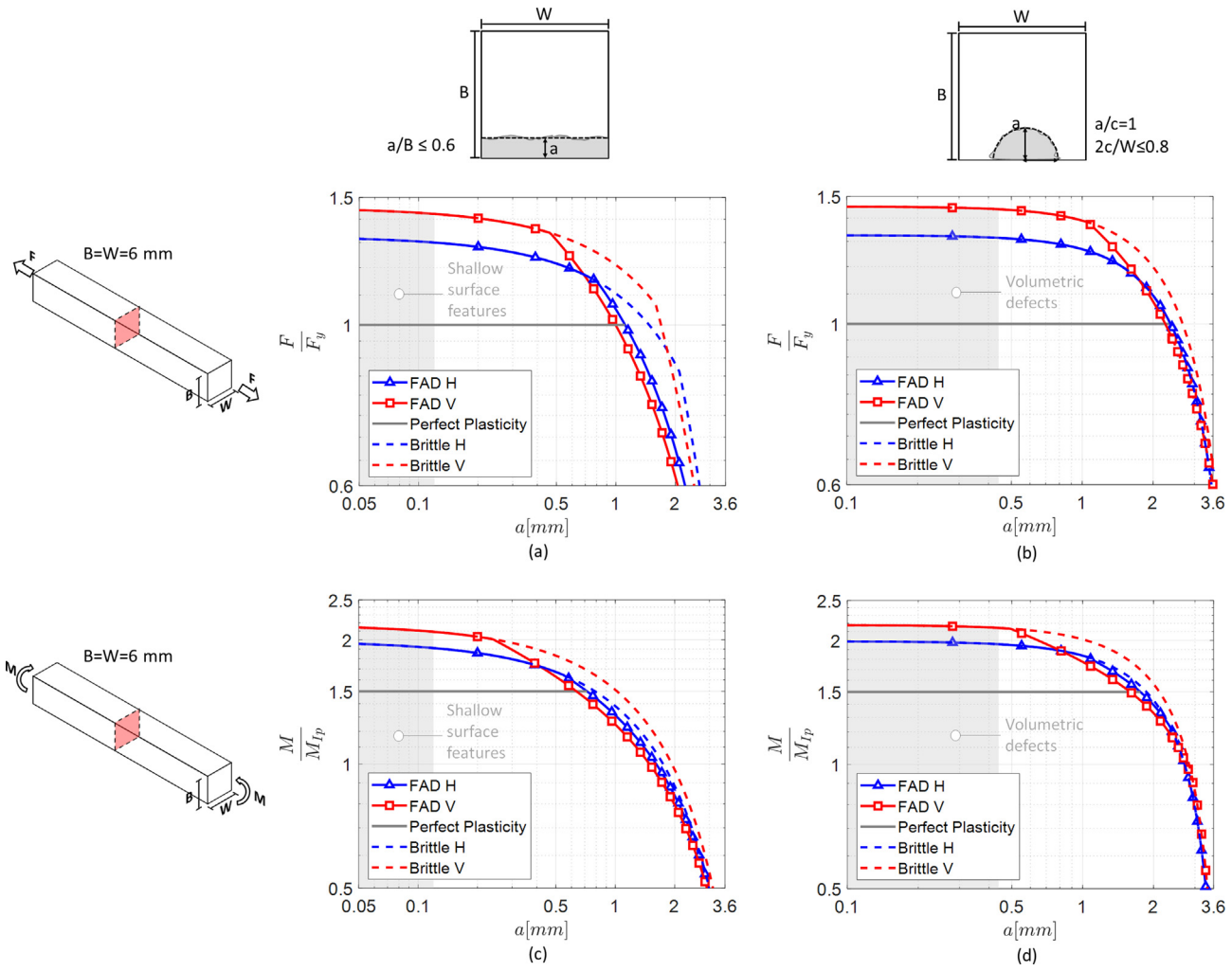

Fig. 16. Limit Load Diagrams for a 6x6 mm AMed AlSi10Mg bar: (a) under tension with a through crack; (b) under tension with a semicircular crack; (c) under pure bending load with a through crack; (d) under pure bending load with a semicircular crack.

ESA [57] and NASA [58] adopt typically two different safety factors: i) a safety factor for yield (FS_Y); ii) a safety factor against the ultimate load (FS_U). As shown in Fig. 15, the identification of the maximum acceptable defect a_p for a given design load is performed as follows:

- the LLD is divided by FS_U to account for the limit on the ultimate load;
- the upper bound on design load is drawn as the horizontal $1/FS_Y$ line, which accounts for the safety factor for yield;
- the maximum acceptable defect a_p is identified as the point on the shifted LLD corresponding to the selected design load.

7.1. Design allowables

The LLD was derived for a bar in AlSi10Mg with a square section having $B = W$=6 mm, for two different load cases, tension and pure bending, and two types of defects, shallow (Fig. 16)) semi-circular flaws (Fig. 16(b, d)). The limit load was normalised by the first-yield load of the non-cracked section of the substitute geometry (identified as F_y for the tension loading case and M_{lp} for the pure bending case). In Fig. 16, the dashed lines correspond to fracture assessment for an ideally brittle material based on the condition $K = K_{mat}$ (valid only in the absence of significant plasticity at the crack tip). It can be observed that, for a given axial load or bending moment, the limit defect for fracture would be larger than the limit defect calculated with the elastic–plastic flaw assessment. The differences between H and V orientation is evident. Differences in the collapse regions are due to the different flow stress to yield strength ratio for the two orientations, while the size of the critical defects in the fracture region is defined by the different fracture toughness values. Considering LLDs for the bending cases, the strain-hardening effect is also appreciable because the bending moment of plastic collapse is approximately twice the bending moment for first yield (while the bending moment of plastic collapse for a perfectly plastic material is $1.5M_{lp}$ [27]). Applying the LLD diagrams and considering safety factors from [57], the allowable defect sizes for design loads/bending moments corresponding to limit values FS_Y=1.1 and FS_U=1.25 are shown in Table 12. Again,

Table 12
Maximum acceptable flaw sizes for a 6 × 6 mm AMed AlSi10Mg bar, printed in the V orientation, under tension/pure bending loads corresponding to limit values FS_Y=1.1 and FS_U=1.25.

Defects - Loads	a_p [mm]	
	Elastic–Plastic $J = J_{mat}$	Brittle $K = K_{mat}$
Shallow - Tension	0.75	1.31
Shallow - Bending	1.20	1.67
Semi-circular - Tension	1.79	2.23
Semi-circular - Bending	2.47	2.66

the data show the need of accounting for material elastic–plastic behaviour for a safe assessment of a prospective component.

7.2. Acceptability of L-PBF anomalies for AlSi10Mg under static loads

It is interesting to adopt the LLD diagrams for discussing the acceptability of the typical defects due to L-PBF manufacturing.

As for surface features, typical of the net-shape surfaces, it has been show that their effect in fatigue is similar to a shallow crack [59]. Considering the sizes of surface features measured in [12] on the 3 PB specimens here tested, the equivalent depth for the surface features can be calculated from their size expressed by $\sqrt{area}$ [60]. In details, the depth for the maximum surface features ranges from 30 μm to 130 μm (largest defects on downfacing surfaces printed at 135°).

For volumetric defects, the scheme of surface semicircular flaw can be taken. Measurements available in [9] show a maximum size internal defects with $\sqrt{area} = 550\,\mu m$ (a value largerly exceeding defects sizes in more recent investigations) from which the maximum crack depth can be calculated as $a_{max} = 440\,\mu m$.

By reporting those ranges on the LLDs (grey areas in Fig. 16), it can be seen that the size of the typical manufacturing defects correspond to the limit load for plastic collapse of the AM parts. Therefore, those defects are not expected to have a significant effect on the static properties (at least if the AM parts have thicknesses/dimensions significantly larger than the defects).

8. Concluding remarks

This paper considers the static assessment of AlSi10Mg components manufactured by L-PBF. In the first part, static fracture tests were performed on two benchmark geometries representing typical AM components: thin plates loaded in tension and notched components subjected to bending. In the second part of the work, the experimental results obtained on the benchmark specimens were compared with results from numerical (FE) and analytical (FAD) models.

The following conclusions can be drawn:

- Despite the low ductility and a quasi-brittle behaviour of AlSi10Mg manufactured by L-PBF, the use of linear-elastic fracture mechanics leads to non-conservative static assessments of the benchmark geometries considered in this study, while the static assessment based on the elastic–plastic fracture mechanics parameter's J-integral provided good estimates on the fracture behaviour;
- By employing adequate SIF solutions, the FAD, originally elaborated only for application to ductile materials, was able to predict the static failures of thin plates well, while it generally yielded slightly conservative predictions for the 3 PB specimens.
- The analytical approximation of elastic–plastic crack driving force provided by the FAD is able to generate useful Limit Load Diagrams to obtain the maximum acceptable defect for a given design load.

Declaration of Competing Interest

The authors declare that they have no known competing financial interests or personal relationships that could have appeared to influence the work reported in this paper.

Acknowledgements

The authors would like to thank BEAMIT (Fornovo, Italy) for preparing the specimens tested in this research. The Italian Ministry of Education, University and Research is also acknowledged for the support provided through the Project "Department of Excellence LIS4.0 - Lightweight and Smart Structures for Industry 4.0". The present work was partally supported by ESA's "IAMSPACE – Italy for Additive Manufacturing in SPACE" project, contract number 4000129932/20/NL/AR.

Appendix A. Material characterization

A.1. Standard specimens geometries and orientations

The tensile cylindrical specimens had a circular cross section with nominal diameter of 3 mm and all the other dimensions were selected according to the ASTM E8 standard [44]. The CT geometry was selected for measuring the fracture toughness. The thickness of the CT specimens was B = 12.4 mm, while the width to thickness ratio was W/B = 2. The notch depth was approximately 12 mm. The H orientation was determined with the loading axis of the tensile specimens to be parallel to the building platform (0°). Accordingly, the H orientation for the CT specimens was defined with the loading axis and the crack plane's normal to be both parallel to the building platform. The vertical (V) orientation determined the loading axes of the tensile and CT specimens to be perpendicular to the building platform (90°). The crack plane's normal was perpendicular to the building platform as well and the crack extension was then expected to be parallel to the layers. The third orientation investigated was the diagonal (D) one, which was characterised by an inclination of 45° between the loading axes and the building platform. A summary of the specimens, per batch and orientation, is provided in Table A.1.

A.2. Standard specimens tests

Material characterization tests were carried out at room temperature, in air. The tensile tests were performed according to the ASTM E8 standard [44] on an MTS Alliance RT 100 load frame, equipped with a 100 kN load cell. The strain was measured with an MTS extensometer with 8 mm gauge length. The fracture toughness tests were conducted according to the ASTM E1820 standard [45] by adopting the resistance curve (R-curve) method. The fracture toughness tests were carried out on an MTS 810 machine equipped with a 10 kN load cell and an MTS clip-on gauge with a nominal length of 5 mm. Before the tests, all specimens were sub-

Table A.1
Experimental planning for tensile and fracture toughness properties.

Test	Type of specimen	Orientation	Batch	Number of tests	Total
Tensile	Cylinder	H (0°)	Batch 1	3	
		V (90°)		3	
		D (45°)		3	9
Fracture toughness	Compact tension CT	H (0°)	Batch 1	2	
			Batch 2	3	
		V (90°)	Batch 1	2	
			Batch 2	2	
		D (45°)	Batch 1	1	10

jected to fatigue load cycling with decreasing Stress Intensity Factor (SIF) range ΔK at constant load ratio R = 0.1 to produce fatigue cracks with a length of approximately 2 mm. After the tests conducted in load control, images of the fracture surfaces were captured by means of a 2 Megapixel Allied Vision Manta CCD camera equipped with a lens system produced by Navitar. The fractographies were used to measure the pre-crack and the final crack lengths after specimens failure.

Fig. A.1 shows the R-curves obtained for CT specimens on the H, V and D orientations for Batches 1 and 2. The dashed black lines corresponds to the blunting lines shifted by Δa=0.2 mm and their intersections with the R-curves represent the J_Q values. The slope of the blunting lines is equal to $2\sigma_{flow}$, where $\sigma_{flow} = (R_{p,0.2\%} + R_m)/2$ is the flow stress, and it's approximately 600 (N/mm)/mm for this AlSi10Mg. It is important to point out that the optically measured physical crack lengths did not conform to the prescriptions on the crack front shape contained in the ASTM E1820 [45] standard, hence the J_Q values could not be qualified as J_{IC}. Non-conformity of the crack front shapes may be related to the absence of side-grooves on the CT specimens. In fact, a marked tunnelling effect was observed in the test region for the two surface points out of the nine points defining the final physical crack length a_f. The deviation of the nine points of a_f was calculated as:

$$deviation = |\bar{a_f} - 0.1 * \sqrt{b_0 \cdot B}| \tag{A.1}$$

where $\bar{a_f}$ is the average of the nine measured points, calculated as per ASTM E1820, and b_0 is the length of the ligament ($b_0 = W - a_0 \approx$11.5 mm, having an initial physical crack length $a_0 \approx$13.5 mm). For each specimen, the maximum deviation is reported in Table A.2 alongside J_Q and K_{J_Q} (calculated from Eq. 2). Nonetheless, the values of J_Q obtained were comparable to J_{IC} values in the literature [11,49,51]. Therefore, J_Q values were used as the reference material fracture toughness J_{mat} in all the subsequent analyses.

Appendix B. Crack characterisation and failure bending moments of 3 PB specimens

Fig. B.1 and Tables B.1, B.2, B.3, B.4.

Table A.2
Maximum deviation of final crack lengths from the prescription of ASTM E1820 for the CT specimens, calculated with Eq. A.1.

Specimen ID	Maximum deviation [mm]	J_Q [N/mm]	K_{J_Q} [MPa]
H1	0.27	8.9	26.7
H2	0.03	8.8	27.1
V1	-	3.7	17.2
V2	0.44	4.6	18.9
D1	0.41	4.6	18.2
H1	0.56	11.2	29.7
H2	0.28	11.2	29.8
H3	0.81	11.3	30.5
V1	0.17	7.9	25.2
V2	0.55	7.3	24.0

Appendix C. Analytical formulations for FAD and CDF analyses

A large number of analytical solutions for SIF and yield loads are available in literature for simple component and crack geometries under generic stress distributions. The main reference used for these analyses was BS 7910 [29].

C.1. Analytical SIF

For thin plates, the following SIF equation from [43] was used:

$$K = Y \cdot S \cdot \sqrt{\pi a} \tag{C.1}$$

Where:

$$Y = \frac{1.12 + \alpha(2.91\alpha - 0.64)}{1 - 0.93\alpha} \tag{C.2}$$

$$S = \frac{Load}{WB} \tag{C.3}$$

$$\alpha = \frac{a}{W} \tag{C.4}$$

Values of W, B and a for each specimen are reported in Table 2.

As regards the 3 PB specimens, different SIF solutions were used. The substitute geometry was a plate with 6x6 mm section (W = B = 6 mm) subjected to pure bending. In most cases, crack geometries were re-characterised starting from the categories defined in Fig. B.1 in B, in order to apply the analytical equations.

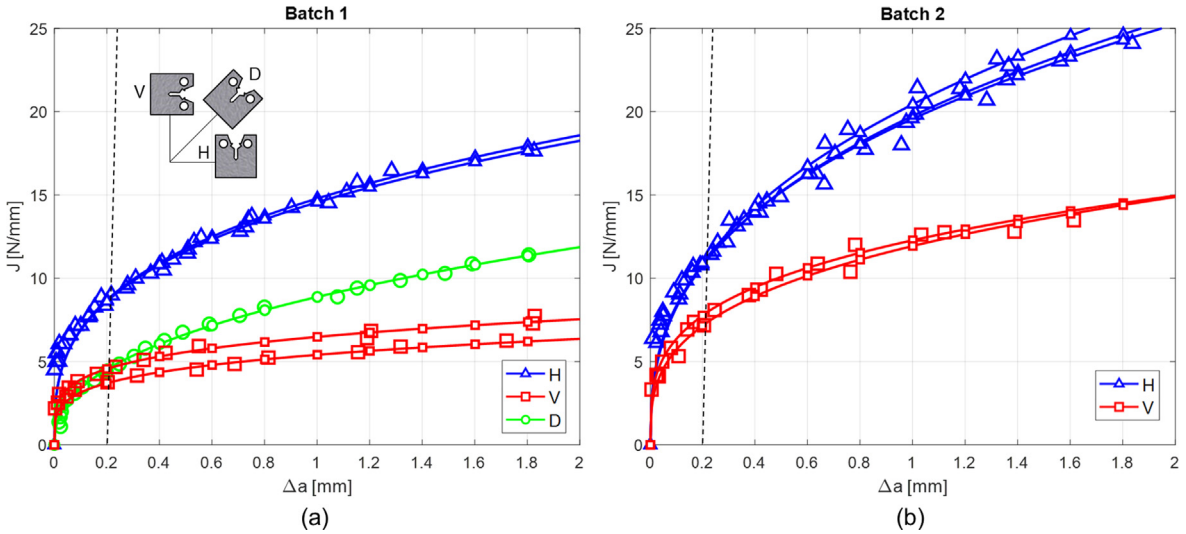

Fig. A.1. R-curves obtained using CT specimens from: (a) Batch 1; (b) Batch 2.

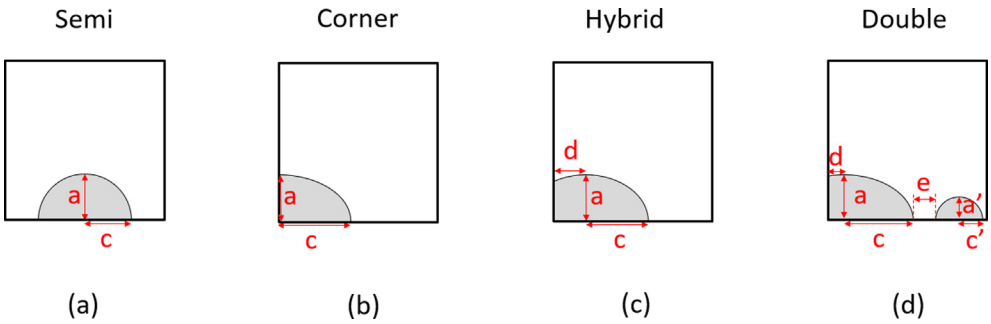

Fig. B.1. Crack categories of 3 PB specimens: (a) Semi-elliptical cracks centred and not centred; (b) Corner cracks; (c) Hybrid cracks, intermediate between Semi-elliptical and Corner; (d) Double cracks.

Table B.1
Crack dimensions and failure bending moments for the "Semi" 3 PB specimens (Fig. B.1(a)).

Specimen	a [mm]	c [mm]	M_f [N·mm]	M_{FAD} [N·mm]
A1	1.76	1.73	11878	11937
A7	1.77	1.82	13179	11729
B2	1.76	3.08	13188	9010
B5	1.62	2.83	12716	10038
B7	1.6	2.85	12080	10057
C6	1.83	2.57	9470	8433
C10	1.26	1.77	11356	11597
C13	1.4	1.64	12558	11317
D14	1.42	2.35	11547	10095
E6	2.01	2.18	10319	8716
E13	1.85	2.22	10331	8999

Table B.2
Crack dimensions and failure bending moments for the "Corner" 3 PB specimens (Fig. B.1(b)).

Specimen	a [mm]	c [mm]	M_f [N·mm]	M_{FAD} [N·mm]
A4	2.26	4.33	12308	9947
B3	1.82	4.09	13043	11296
B6	2.43	3.92	12976	9930
C8	2.6	3.55	10098	8486
C12	2.51	3.73	10002	8480
D7	1.45	6	9807	8461

Table B.3
Crack dimensions and failure bending moments for the "Hybrid" 3 PB specimens (Fig. B.1(c)).

Specimen	a [mm]	c [mm]	d [mm]	M_f [N·mm]	M_{FAD} [N·mm]
A2	1.83	2.48	2.25	11688	11720
A5	2.45	3.19	0.85	12296	10305
A8	1.8	2.97	2.32	11935	11167
A9	2.06	3.04	1.93	12125	11031
B4	1.74	2.77	2.28	12654	11481
B8	1.56	3.11	2.41	12896	11382
B14	2.76	5.02	-0.6	11470	10002
C9	1.22	2.66	2.17	11061	10686
C11	2.19	4.63	-1.69	12399	10258
D6	1.77	4.07	1.82	9972	8746
D10	1.66	3.32	2.42	9378	9243
E7	2.03	3.13	2.88	9205	8635
E9	2.19	3.34	0.59	9887	9217
E10	2.32	3.06	0.75	9828	9080
E11	2.08	3.09	0.76	10438	9599
E12	2.19	3.5	0.81	10299	9043

Table B.4
Crack dimensions and failure bending moments for the "Double" 3 PB specimens (Fig. B.1(d)).

Specimen	a [mm]	c [mm]	d [mm]	e [mm]	a' [mm]	c' [mm]	M_f [N·mm]	M_{FAD} [N·mm]
D13	1.39	2.33	0.92	0.65	0.82	0.92	11970	11289
E14	1.81	2.82	1.64	0.88	0.54	0.57	10057	8093

Details on the re-characterisation and on the reference solutions used are as follows:

- "Semi" cracks were all treated as centred surface defects with semi-elliptical shape. Results reported in Fig. 11, 12 and Table 11 were obtained using SIF solution M 4.1 from BS7910:2019, which is based on [32]. Results reported in Table B.1, on the other hand, were obtained using SIF solutions from [61].
- "Corner" and "Hybrid" cracks were all re-characterised as corner cracks with the same crack depth a and crack half-width equal to $c + d$ (Table B.2, B.3), and then SIF solutions from [62] were used.
- "Double" cracks were recharacterised as semi-elliptical cracks with crack depth a and crack width equal to $c + d+e + 2c\prime$ (Table B.4), and then SIF solutions from [61] were used.

For all cases, the SIF was calculated for both the deepest point and for the point on the surface of the crack. The maximum SIF between the two points investigated was then used to calculate the failure bending moment.

C.2. Analytical yield load

Several types of yield loads may be defined for a cracked component. The yield load considered in this work was the local plastic collapse of the net section, defined as the load for which the cracked ligament of the component is fully plasticised [29].

For thin plates, the plastic collapse load F_{pc} was simply obtained as the yield strength $R_{p,0.2\%}$ multiplied by the net area of the cracked ligament A_{net}:

$$F_{pc} = A_{net} \cdot R_{p,0.2\%} \tag{C.5}$$

For the 3 PB specimens, the bending moment of plastic collapse M_{pc} was obtained considering the first moment of area of the cracked ligament. The starting step was to calculate the area and the centre of mass of the crack, from which it was possible to define the centre of mass of the cracked ligament, and thus the neutral axis of the section. Calculating the areas A and centres of mass y of the tensioned (A_t, y_t) and compressed (A_c, y_c) part of the cracked ligament enabled us to obtain the plastic section modulus:

$$Z = A_c \cdot y_c + A_t \cdot y_t \tag{C.6}$$

The bending moment of plastic collapse was finally obtained as:

$$M_{pc} = Z \cdot R_{p,0.2\%} \tag{C.7}$$

This procedure is based on the hypothesis of pure bending applied to a symmetrical section. However, in this work, most cracks were "Corner" or "Hybrid", hence with asymmetric cracked section. The approach followed for "Corner" and "Hybrid" cracks was to treat the crack shape as semi-elliptical, using the a and c values identified (Table B.1, B.2, B.3, B.4) and to double the thickness W of the section. In this way, all the sections could be considered symmetrical and the calculation of the bending moments of plastic collapse was straightforward.

References

[1] T.D. Ngo, A. Kashani, G. Imbalzano, K.T. Nguyen, D. Hui, Additive manufacturing (3D printing): A review of materials, methods, applications and challenges, Compos. Part B: Eng. 143 (2018) 172–196, https://doi.org/10.1016/j.compositesb.2018.02.012.

[2] S.L. Sing, J. An, W.Y. Yeong, F.E. Wiria, Laser and electron-beam powder-bed additive manufacturing of metallic implants: A review on processes, materials and designs, J. Orthop. Res. 34 (3) (2016) 369–385.

[3] D.E. Cooper, M. Stanford, K.A. Kibble, G.J. Gibbons, Additive manufacturing for product improvement at red bull technology, Mater. Des. 41 (2012) 226–230.

[4] L. Nickels, Am and aerospace: an ideal combination, Met. Powder Rep. 70 (6) (2015) 300–303.

[5] A. Uriondo, M. Esperon-Miguez, S. Perinpanayagam, The present and future of additive manufacturing in the aerospace sector: A review of important aspects, Proc. Inst. Mech. Eng., Part G: J. Aeros. Eng. 229 (11) (2015) 2132–2147.

[6] R. Liu, Z. Wang, T. Sparks, F. Liou, J. Newkirk, Aerospace applications of laser additive manufacturing, in: Laser additive manufacturing, Elsevier, 2017, pp. 351–371.

[7] W. Li, S. Li, J. Liu, A. Zhang, Y. Zhou, Q. Wei, C. Yan, Y. Shi, Effect of heat treatment on AlSi10Mg alloy fabricated by selective laser melting: Microstructure evolution, mechanical properties and fracture mechanism, Mater. Sci. Eng., A 663 (2016) 116–125, https://doi.org/10.1016/j.msea.2016.03.088.

[8] S. Beretta, S. Romano, A comparison of fatigue strength sensitivity to defects for materials manufactured by AM or traditional processes, Int. J. Fatigue 94 (2017) 178–191, https://doi.org/10.1016/j.ijfatigue.2016.06.020.

[9] S. Romano, A. Brückner-Foit, A. Brandão, J. Gumpinger, T. Ghidini, S. Beretta, Fatigue properties of AlSi10Mg obtained by additive manufacturing: Defect-based modelling and prediction of fatigue strength, Eng. Fract. Mech. 187 (2018) 165–189, https://doi.org/10.1016/j.engfracmech.2017.11.002.

[10] J. Zhang, B. Song, Q. Wei, D. Bourell, Y. Shi, A review of selective laser melting of aluminum alloys: Processing, microstructure, property and developing trends, J. Mater. Sci. Technol. 35 (2) (2019) 270–284, https://doi.org/10.1016/j.jmst.2018.09.004.

[11] Q. Liu, H. Wu, M.J. Paul, P. He, Z. Peng, B. Gludovatz, J.J. Kruzic, C.H. Wang, X. Li, Machine-learning assisted laser powder bed fusion process optimization for AlSi10Mg: New microstructure description indices and fracture mechanisms, Acta Mater. 201 (2020) 316–328, https://doi.org/10.1016/j.actamat.2020.10.010.

[12] S. Beretta, M. Gargourimotlagh, S. Foletti, A. du Plessis, M. Riccio, Fatigue strength assessment of "as built" AlSi10Mg manufactured by SLM with different build orientations, Int. J. Fatigue 139 (2020) 105737, https://doi.org/10.1016/j.ijfatigue.2020.105737.

[13] K.V. Yang, P. Rometsch, T. Jarvis, J. Rao, S. Cao, C. Davies, X. Wu, Porosity formation mechanisms and fatigue response in al-si-mg alloys made by selective laser melting, Materials Science and Engineering: A 712 (2018) 166–174, https://doi.org/10.1016/j.msea.2017.11.078. URL https://www.sciencedirect.com/science/article/pii/S0921509317315393.

[14] N.T. Aboulkhair, M. Simonelli, L. Parry, I. Ashcroft, C. Tuck, R. Hague, 3d printing of aluminium alloys: Additive manufacturing of aluminium alloys using selective laser melting, Progress in materials science 106 (2019) 100578.

[15] A. Mostafaei, C. Zhao, Y. He, S. Reza Ghiaasiaan, B. Shi, S. Shao, N. Shamsaei, Z. Wu, N. Kouraytem, T. Sun, J. Pauza, J.V. Gordon, B. Webler, N.D. Parab, M. Asherloo, Q. Guo, L. Chen, A.D. Rollett, Defects and anomalies in powder bed fusion metal additive manufacturing, Current Opinion in Solid State and Materials Science 26 (2). doi: 10.1016/j.cossms.2021.100974. https://www.sciencedirect.com/science/article/pii/S1359028621000772.

[16] E. Brandl, U. Heckenberger, V. Holzinger, D. Buchbinder, Additive manufactured AlSi10Mg samples using Selective Laser Melting (SLM): Microstructure, high cycle fatigue, and fracture behavior, Materials & Design 34 (2012) 159–169, https://doi.org/10.1016/j.matdes.2011.07.067.

[17] Z. Xu, A. Liu, X. Wang, Fatigue performance and crack propagation behavior of selective laser melted AlSi10Mg in 0°, 15°, 45° and 90° building directions, Materials Science and Engineering: A 812. doi:10.1016/j.msea.2021.141141.

[18] P. Nezhadfar, S. Thompson, A. Saharan, N. Phan, N. Shamsaei, Structural integrity of additively manufactured aluminum alloys: Effects of build orientation on microstructure, porosity, and fatigue behavior, Additive Manufacturing 47. doi:10.1016/j.addma.2021.102292.

[19] U. Zerbst, G. Bruno, J.-Y. Buffière, T. Wegener, T. Niendorf, T. Wu, X. Zhang, N. Kashaev, G. Meneghetti, N. Hrabe, M. Madia, T. Werner, K. Hilgenberg, M. Koukolíková, R. Procházka, J. Džugan, B. Möller, S. Beretta, A. Evans, R. Wagener, K. Schnabel, Damage tolerant design of additively manufactured metallic components subjected to cyclic loading: State of the art and challenges, Progress in Materials Sciencedoi:10.1016/j.pmatsci.2021.100786.

[20] ECSS-E-ST-32-01C Rev.2 - Fracture Control, Tech. rep., Noordwijk, NL (2021).

[21] D. Buchbinder, H. Schleifenbaum, S. Heidrich, W. Meiners, J. Bültmann, High Power Selective Laser Melting (HP SLM) of Aluminum Parts, Physics Procedia 12 (2011) 271–278, https://doi.org/10.1016/j.phpro.2011.03.035.

[22] I. Rosenthal, E. Tiferet, M. Ganor, A. Stern, Post-Processing of AM-SLM AlSi10Mg Specimens: Mechanical Properties and Fracture Behaviour, The Annals of Dunarea de Jos University of Galati, Fascicle XII: Welding Equipment and Technology 26 (2015) 33–38.

[23] A.A. Raus, M.S. Wahab, M. Ibrahim, K. Kamarudin, A. Aqeel, S. Shamsudin, Mechanical and Physical Properties of AlSi10Mg Processed through Selective Laser Melting, International Journal of Engineering and Technology 8 (6) (2016) 2612–2618, https://doi.org/10.21817/ijet/2016/v8i6/160806217.

[24] E. Sert, E. Schuch, A. Öchsner, L. Hitzler, E. Werner, M. Merkel, Tensile strength performance with determination of the Poisson's ratio of additively manufactured AlSi10Mg samples, Materialwiss. Werkstofftech. 50 (5) (2019) 539–545, https://doi.org/10.1002/mawe.201800233.

[25] L. Hitzler, C. Janousch, J. Schanz, M. Merkel, B. Heine, F. Mack, W. Hall, A. Öchsner, Direction and location dependency of selective laser melted AlSi10Mg specimens, J. Mater. Process. Technol. 243 (2017) 48–61, https://doi.org/10.1016/j.jmatprotec.2016.11.029.

[26] S. AlRedha, A. Shterenlikht, M. Mostafavi, D. Van Gelderen, O.E. Lopez-Botello, L.A. Reyes, P. Zambrano, C. Garza, Effect of build orientation on fracture behaviour of AlSi10Mg produced by selective laser melting, Rapid Prototyping Journal 27 (1) (2021) 112–119, https://doi.org/10.1108/RPJ-02-2020-0041.

[27] N.E. Dowling, Mechanical Behavior of Materials: Engineering Methods for Deformation, Fracture, and Fatigue, 4th Edition., Pearson, Harlow, 2013.
[28] T.L. Anderson, Fracture Mechanics: Fundamentals and Applications, 3rd Edition., Taylor & Francis, Boca Raton, FL, 2005.
[29] BS 7910: Guide to methods for assessing the acceptability of flaws in metallic structures (2019).
[30] British Energy Generation Ltd, R6 Revision 4: Assessment of the Integrity of Structures Containing Defects (2020).
[31] API 579: Recommended Practice for Fitness for Service (2000).
[32] J.C.J. Newman, I.S. Raju, Stress-Intensity Factor Equations for Cracks in Three-Dimensional Finite Bodies Subjected to Tension and Bending Loads (1986) 311–334.
[33] C.F. Shih, J.W. Hutchinson, Fully Plastic Solutions and Large Scale Yielding Estimates for Plane Stress Crack Problems, J. Eng. Mater. Technol. 98 (4) (1976) 289–295, https://doi.org/10.1115/1.3443380.
[34] U. Zerbst, M. Schödel, S. Webster, R. Ainsworth, Fitness-for-Service Fracture Assessment of Structures Containing Cracks, Academic Press, 2007.
[35] U. Zerbst, K.-H. Schwalbe, R. Ainsworth, An Overview of Failure Assessment Methods in Codes and Standards, Comprehensive Structural Integrity, Elsevier, 2003, pp. 1–48, https://doi.org/10.1016/B0-08-043749-4/07053-1.
[36] I. Hadley, BS 7910:2013 in brief, Int. J. Press. Vessels Pip. 165 (2018) 263–269, https://doi.org/10.1016/j.ijpvp.2018.07.010.
[37] T. Iwashita, Y. Kurobane, K. Azuma, Y. Makino, Prediction of brittle fracture initiating at ends of cjp groove welded joints with defects: study into applicability of failure assessment diagram approach, Engineering structures 25 (14) (2003) 1815–1826.
[38] M. Seifi, A. Salem, J. Beuth, O. Harrysson, J.J. Lewandowski, Overview of materials qualification needs for metal additive manufacturing, Jom 68 (3) (2016) 747–764.
[39] U. Zerbst, G. Bruno, J.-Y. Buffiere, T. Wegener, T. Niendorf, T. Wu, X. Zhang, N. Kashaev, G. Meneghetti, N. Hrabe, et al., Damage tolerant design of additively manufactured metallic components subjected to cyclic loading: State of the art and challenges, Progress in materials science 121 (2021) 100786.
[40] M. Gorelik, Additive manufacturing in the context of structural integrity, Int. J. Fatigue 94 (2017) 168–177.
[41] ECSS-Q-ST-70-80C - Space product assurance: Processing and quality assurance requirements for metallic powder bed fusion technologies for space applications, Tech. rep., Noordwijk, NL (2021).
[42] ASTM International, Standard Test Methods for Density of Compacted or Sintered Powder Metallurgy (PM) Products Using Archimedes' Principle (2017). doi: 10.1520/B0962-17.
[43] H. Tada, P.C. Paris, G.R. Irwin, The Stress Analysis of Cracks Handbook, 3rd Edition., ASME Press, New York, 2000.
[44] ASTM E8/E8M-21 Standard Test Methods for Tension Testing of Metallic Materials (2021). https://www.astm.org/Standards/E8.
[45] ASTM E1820–20b Standard Test Method for Measurement of Fracture Toughness (2020). https://www.astm.org/Standards/E1820.
[46] N. Read, W. Wang, K. Essa, M.M. Attallah, Selective laser melting of AlSi10Mg alloy: Process optimisation and mechanical properties development, Materials & Design (1980–2015) 65 (2015) 417–424. doi:10.1016/j.matdes.2014.09.044.
[47] K. Kempen, L. Thijs, J. Van Humbeeck, J.-P. Kruth, Processing AlSi10Mg by selective laser melting: parameter optimisation and material characterisation, Mater. Sci. Technol. 31 (8) (2015) 917–923, https://doi.org/10.1179/1743284714Y.0000000702.
[48] L. Hitzler, N. Schoch, B. Heine, M. Merkel, W. Hall, A. Öchsner, Compressive behaviour of additively manufactured AlSi10Mg, Materialwiss. Werkstofftech. 49 (5) (2018) 683–688, https://doi.org/10.1002/mawe.201700239.
[49] M.J. Paul, Q. Liu, J.P. Best, X. Li, J.J. Kruzic, U. Ramamurty, B. Gludovatz, Fracture resistance of AlSi10Mg fabricated by laser powder bed fusion, Acta Materialia 211. doi:10.1016/j.actamat.2021.116869.
[50] L. Zhao, L. Song, J.G.S. Macías, Y. Zhu, M. Huang, A. Simar, Z. Li, Review on the Correlation Between Microstructure and Mechanical Performance for Laser Powder Bed Fusion AlSi10Mg, Additive Manufacturingdoi:10.1016/j.addma.2022.102914. https://linkinghub.elsevier.com/retrieve/pii/S2214860422003116.
[51] L.C. Araújo, A.H. Gabriel, E.B. da Fonseca, J.A. Avila, A.L. Jardini, R.S. Junior, É. S. Lopes, Effects of build orientation and heat treatments on the tensile and fracture toughness properties of additively manufactured AlSi10Mg, International Journal of Mechanical Sciencesdoi:10.1016/j.ijmecsci.2021.106868.
[52] L. Hitzler, J. Hirsch, J. Schanz, B. Heine, M. Merkel, W. Hall, A. Öchsner, Fracture toughness of selective laser melted AlSi10Mg, Proceedings of the Institution of Mechanical Engineers, Part L: Journal of Materials: Design and Applications 233 (4) (2019) 615–621, https://doi.org/10.1177/1464420716687337.
[53] J.T. Oliveira de Menezes, E.M. Castrodeza, R. Casati, Effect of build orientation on fracture and tensile behavior of A357 Al alloy processed by Selective Laser Melting, Materials Science and Engineering: A 766. doi:10.1016/j.msea.2019.138392.
[54] D.S. Dugdale, Yielding of steel sheets containing slits, J. Mech. Phys. Solids 8 (2) (1960) 100–104.
[55] M. Gupta, R. Alderliesten, R. Benedictus, A review of t-stress and its effects in fracture mechanics, Eng. Fract. Mech. 134 (2015) 218–241, https://doi.org/10.1016/j.engfracmech.2014.10.013. URL https://www.sciencedirect.com/science/article/pii/S001379441400335X.
[56] R.A. Ainsworth, I. Sattari-Far, A.H. Sherry, D.G. Hooton, I. Hadley, Methods for including constraint effects within the SINTAP procedures, Eng. Fract. Mech. 67 (6) (2000) 563–571, https://doi.org/10.1016/S0013-7944(00)00074-6. URL https://www.sciencedirect.com/science/article/pii/S0013794400000746.
[57] ECSS-E-ST-32-10C Rev.2 - Structural factors of safety for spaceflight hardware, Tech. rep., Noordwijk, NL (2019).
[58] McElroy, A Summary of NASA-HDBK-5026: Guidance on strength, fatigue, and fracture control requirements for additive manufactured spaceflight hardware, Presentation at ICAM 2021, available at: https://ntrs.nasa.gov/citations/20210020710 (2021). https://ntrs.nasa.gov/citations/20210020710.
[59] A. Du Plessis, S. Beretta, Killer notches: The effect of as-built surface roughness on fatigue failure in alsi10mg produced by laser powder bed fusion, Additive Manufacturing 35 (2020) 101424.
[60] Y. Murakami, Metal fatigue: effects of small defects and nonmetallic inclusions, Academic Press, 2019.
[61] I.S. Raju, S. Mettu, V. Shivakumar, Stress intensity factor solutions for surface cracks in flat plates subjected to nonuniform stresses, Fract. Mech.:Twenty-Fourth Volume, ASTM STP 1207 (1994) 560–580.
[62] I.S. Raju, J.C. Newman, Stress-intensity factors for corner cracks in rectangular bars, Fract. Mech.: Nineteenth Symposium, ASTM STP 969 (1988) 43–55.